TURBULENT CONVECTION IN STELLAR INTERIORS. I. HYDRODYNAMIC SIMULATION

Casey A. Meakin[1,2] and David Arnett[1]

ABSTRACT

We describe the results of 3D numerical simulations of oxygen shell burning and hydrogen core burning in a 23 $M_\odot$ stellar model. A detailed comparison is made to stellar mixing-length theory (MLT) for the shell-burning model. Simulations in 2D are significantly different from 3D, in terms of both flow morphology and velocity amplitude. Convective mixing regions are better predicted using a *dynamic boundary condition* based on the bulk Richardson number than by purely local, static criteria like Schwarzschild or Ledoux. MLT gives a good description of the velocity scale and temperature gradient for shell convection; however, there are other important effects that it does not capture, mostly related to the dynamical motion of the boundaries between convective and nonconvective regions. There is asymmetry between upflows and downflows, so the net kinetic energy flux is not zero. The motion of convective boundaries is a source of gravity waves; this is a necessary consequence of the deceleration of convective plumes. Convective "overshooting" is best described as an elastic response by the convective boundary, rather than ballistic penetration of the stable layers by turbulent eddies. The convective boundaries are rife with internal and interfacial wave motions, and a variety of instabilities arise that induce mixing through a process best described as turbulent entrainment. We find that the rate at which material entrainment proceeds at the boundaries is consistent with analogous laboratory experiments and simulation and observation of terrestrial atmospheric mixing. In particular, the normalized entrainment rate $E = u_E/\sigma_H$ is well described by a power-law dependence on the bulk Richardson number $\text{Ri}_B = \Delta bL/\sigma_H^2$ for the conditions studied, $20 \lesssim \text{Ri}_B \lesssim 420$. We find $E = A\text{Ri}_B^{-n}$, with best-fit values $\log A = 0.027 \pm 0.38$ and $n = 1.05 \pm 0.21$. We discuss the applicability of these results to stellar evolution calculations.

Subject headings: hydrodynamics — instabilities — nuclear reactions, nucleosynthesis, abundances — stars: evolution — stars: general — stars: interiors — supernovae: general — turbulence — waves

1. INTRODUCTION

As a consequence of unresolved discrepancies between stellar evolution models and observations of (1) stellar surface abundances (e.g., Lattanzio & Lugaro 2005; Pasquini et al. 2004; Charbonnel & Talon 1999) and (2) fundamental stellar parameters (e.g., radius and luminosity; Ribas 2006), there is increasing interest in better understanding the hydrodynamic transport processes operating in stellar interiors. Often, observation and theory can be brought into better agreement through the application of additional mixing. However, the current descriptions of mixing used in evolution codes are based on woefully incomplete physical models that have parameters that are often calibrated to match a restricted set of observables.

The general approach used to describe stellar mixing, beyond the homogenization of material within convective regions, is to treat it as a diffusive process. For instance, composition is evolved in the Lagrangian frame according to an equation of the form

$$\frac{dX_i}{dt} = \left(\frac{\partial X_i}{\partial t}\right)_{\text{nuc}} + \frac{\partial}{\partial m_r}\left(\hat{D}\frac{\partial X_i}{\partial m_r}\right). \quad (1)$$

The terms on the right-hand side include composition changes due to nuclear burning and diffusive mixing. The physical model of mixing is encapsulated in the Lagrangian diffusion coefficient $\hat{D}$, which is in turn written in terms of the Eulerian one D, as $\hat{D} = (\partial m_r/\partial r)^2 D$. The formulation of the diffusivity D is generally

based on the product of a velocity and length scale $D \sim vl$, or as the ratio of a length scale squared and a timescale $D \sim l^2/\tau$. The length, time, and velocity scales used in calculating D are almost exclusively order-of-magnitude estimates based on linear instability theory. The actual mixing being represented, however, is almost always a nonlinear, turbulent process in reality.

A large number of fluid instabilities have been identified for which diffusion coefficients of the type discussed have been formulated. Examples include rotational instabilities (Pinsonneault et al. 1989), the effects of magnetic torques (Spruit 2002), semiconvection (Langer et al. 1983; Spruit 1992), and internal wave–induced mixing (García López & Spruit 1991; Montalban 1994; Young et al. 2003). A fairly comprehensive discussion of implementing mixing processes in this "diffusive" spirit can be found in Heger et al. (2000, 2005).

Hydrodynamic simulation extends our knowledge of fluid instabilities into the nonlinear regime and provides insight into the transport processes operating throughout a stellar interior. Direct contact between hydrodynamic simulation and stellar evolution modeling is a very recent development and is beginning to mature alongside improved computing capabilities. One of the earliest examples of directly calibrating a one-dimensional (1D) stellar evolution code against the results of a multidimensional hydrodynamic simulation is the work of Herwig et al. (1997), who examined the impact of mixing on the nucleosynthesis in asymptotic giant branch (AGB) stars. In this work, a diffusion coefficient was used that represented the exponentially decaying "overshoot" velocity field seen in the two-dimensional (2D) convection simulations of Freytag et al. (1996). A growing but still small number of groups are now studying the hydrodynamics of stellar interiors with three-dimensional (3D) simulation. Examples

[1] Steward Observatory, University of Arizona, Tucson, AZ 85721; casey@flash.uchicago.edu, darnett@as.arizona.edu.
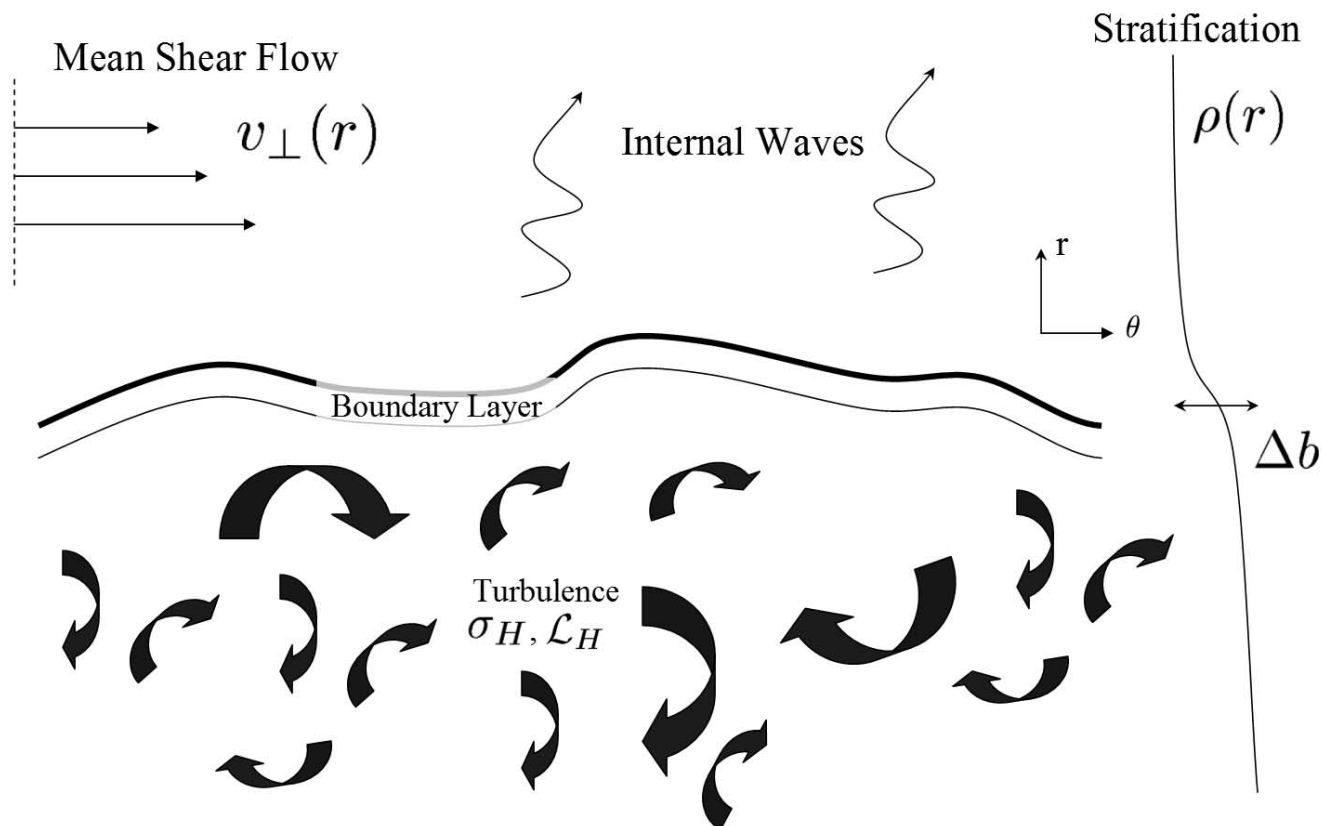[2] FLASH Center, University of Chicago, Chicago, IL 60637.

Fig. 1.—Diagram illustrating the salient features of the density and velocity field for the turbulent entrainment problem. Three layers are present: a turbulent convection zone is separated from an overlying stably stratified region by a boundary layer of thickness h and buoyancy jump $\Delta b \sim N^2 h$. The turbulence near the interface is characterized by integral scale and rms velocity $\mathcal{L}_H$ and σ_H, respectively. The stably stratified layer with buoyancy frequency $N(r)$ propagates internal waves that are excited by the adjacent turbulence. A shear velocity field $v_\perp(r)$, associated with differential rotation, may also be present. After Strang & Fernando (2001).

include simulations of the core helium flash using the full-star modeling code Djehuty (Dearborn et al. 2006; Eggleton et al. 2007) and core carbon burning in a white dwarf (Kuhlen et al. 2006) using anelastic hydrodynamic methods (Glatzmaier 1984).

In this paper we discuss new, fully compressible simulations of 3D, turbulent, thermally relaxed, nearly adiabatic convection (high Péclet number) relevant to deep interior regions in stars (i.e., to most stellar mass that is convective, but not mildly subphotospheric and surface regions). We simulate oxygen shell burning on its natural timescale and core hydrogen burning driven at 10 times its natural rate. The simulations develop a robust quasi-steady behavior in a statistical sense, with significant intermittency. We analyze this statistical behavior quantitatively and compare it to predictions of astrophysical mixing-length theory (MLT; Böhm-Vitense 1958). MLT gives a good representation of many aspects of convection but omits others (especially wave generation and mass entrainment) that are related to the dynamical behavior of stably stratified layers adjacent to the convection.

In § 2 we briefly summarize some results of the study of turbulent entrainment in geophysics, to prepare the reader for its appearance in our astrophysical simulations. This process is not included in the standard approach to stellar evolution (Cox & Giuli 1968; Clayton 1983; Kippenhahn & Weigert 1990; Hansen & Kawaler 1994). In § 3 we discuss our numerical and theoretical tools. In § 4 we present our simulations of oxygen shell burning, which attain a thermal steady state (this is possible because of the rapidity of nuclear heating and neutrino cooling). In § 5 we discuss a less advanced burning stage, core hydrogen burning, which we are able to examine with the use of an artificially en-

hanced hydrogen burning rate (by a factor of 10). We find that the behavior is similar to the oxygen burning shell, suggesting that our results may have broad application for stellar evolution. In § 6 we compare our results to the assumptions of MLT, and in § 7 we show that our results lead to a simple model of turbulent entrainment, an effect not in MLT nor in standard stellar evolutionary calculations.

This paper is the first in a series. In subsequent papers, we incorporate the "empirical" convection model developed in this paper into the TYCHO stellar evolution code (Young & Arnett 2005) and begin to assess its influence on stellar evolution, on nucleosynthetic yields, and on the structure of supernova progenitors.

2. TURBULENT ENTRAINMENT

The presence of a turbulent layer contiguous with a stably stratified layer is common in both astrophysical and geophysical flows. Turbulence in stratified media is often sustained by strong shear flows or thermal convection and bound by a stabilizing density interface. Over time, the turbulent layer "diffuses" into the stable layer and the density interface recedes, thus increasing the size of the mixed region. The basic features of this *turbulent entrainment problem* are illustrated in Figure 1. The rate at which the density interface recedes into the stable layer $u_E = \partial r_i/\partial t$ is called the entrainment rate, and its dependence on the parameters characterizing the turbulent and the stable layers has been the subject of numerous experimental and theoretical studies. This process is generally ignored in stellar evolutionary studies.

Experimental studies have mostly been of "mixing box" type, which involves a tank of fluid with a turbulent layer and a

density-stratified layer. The turbulence is generated by thermal convection or an oscillating wire mesh, and density stratification is imposed by either a solute or thermal gradient (Turner 1980). Complementary to these shear-free mixing box models are shear-driven models. Shear-driven turbulence experiments involve either a recirculation track that propels one layer of fluid above a stationary layer or a rotating plate in contact with the fluid that drives a circulation in the upper layer. Shear instabilities sustain a turbulent mixed layer in the overlying fluid that entrains fluid from the lower, stationary layer (Kantha et al. 1977; Strang & Fernando 2001). In all of these laboratory experiments, a variety of increasingly sophisticated flow visualization techniques are being used to study both the overall entrainment rate u_E and the physical mechanisms that underly the entrainment process.

One of the primary conclusions of these studies is that the entrainment rate depends on a Richardson number, which is a dimensionless measure of the "stiffness" of the boundary relative to the strength of the turbulence. In shear-free turbulent entrainment the bulk Richardson number,

$$\mathrm{Ri}_B = \frac{\Delta b L}{\sigma^2}, \tag{2}$$

is most commonly studied. Here Δb is the buoyancy jump across the interface, σ is the rms turbulence velocity adjacent to the interface, and L is a length scale for the turbulent motions, which is often taken to be the horizontal integral scale of the turbulence near the interface. The relative buoyancy is defined by the integral

$$b(r) = \int_{r_i}^{r} N^2 \, dr, \tag{3}$$

where N is the buoyancy frequency defined by

$$N^2 = -g\left(\frac{\partial \ln \rho}{\partial r} - \frac{\partial \ln \rho}{\partial r}\bigg|_s\right). \tag{4}$$

The entrainment coefficient E is the interface migration speed u_e normalized by the rms turbulent velocity at the interface $E = u_E/\sigma$ and is generally found to obey a power-law dependence on Ri_B,

$$E = A\mathrm{Ri}_B^{-n}. \tag{5}$$

The exponent is usually found to lie in the range $1 \lesssim n \lesssim 1.75$ and has been the subject of many theoretical studies of the entrainment process. Dimensional analysis suggests that Ri_B should be the controlling parameter, so long as microscopic diffusion plays a minor role (Phillips 1966). Basic energetic arguments in which the rate of change of potential energy due to mixing is assumed to be proportional to the turbulent kinetic energy available at the interface lead to an exponent of $n = 1$ (e.g., Linden 1975). This same power-law exponent has also been derived for models of the growth of the planetary boundary layer due to turbulent entrainment by penetrative convection (Stull 1973, 1976a; Tennekes 1973; Sorbjan 1996).

The normalization of the entrainment coefficient A varies significantly between the various laboratory and field studies conducted, with recent values found in the range $0.1 < A < 0.5$ (e.g., Stevens & Bretherton 1999). The discrepancy among the normalization constants has been called the "A-dilemma" (Bretherton et al. 1999). A review (up to 1991) of experimental measures of

the parameters in the entrainment law of equation (5) is tabulated in Fernando (1991), and a recent review of entrainment models used in the atmospheric sciences is discussed by Stevens (2002).

The experimental and theoretical models discussed above are generally motivated by geophysical problems (see, e.g., Lilly 2002a, 2002b) but are directly relevant to the conditions found in stellar interiors. The bulk Richardson numbers that characterize stellar convective boundaries fall within the same parameter range ($10 < \mathrm{Ri}_B < 500$), and the background stratifications possess a similar buoyancy structure, so that geophysical models can serve as a guide to better understand the stellar case.

3. THE NUMERICAL TOOLS

3.1. *One-dimensional Stellar Evolution*

The hydrodynamic simulations that we study in this paper are of two distinct phases in the evolution of a 23 $M_\odot$ supernova progenitor: main-sequence core convection, and convective oxygen shell burning. The initial conditions taken from 1D stellar models evolved with TYCHO (Young & Arnett 2005) an open source stellar evolution code.[3] A choice of standard 1D stellar evolution procedures is used. The MLT as described in Kippenhahn & Weigert (1990) is used with instantaneous mixing of composition in the convectively unstable regions. The limits of the convection zones are determined using the Ledoux criterion, which incorporates the stabilizing effects of composition gradients. Semiconvective mixing has been turned off. Nuclear evolution is followed with a 177 element network using the rates of Rauscher & Thielemann (2000). Opacities are from Iglesias & Rogers (1996) and Alexander & Ferguson (1994) for high- and low-temperature regimes, respectively. The solar abundance of Grevesse & Sauval (1998) are used. Although more recent abundance determinations have been made (Asplund et al. 2005), the impact on the stellar structure of the models presented here is small, and minor variations in the abundances have a negligible influence on the development of the hydrodynamic flow.

3.2. *Multidimensional Reactive Hydrodynamics with PROMPI*

The core of our multidimensional hydrodynamics code is the solver written by Fryxell et al. (1991), which is based on the direct Eulerian implementation of the piecewise parabolic method (PPM; Colella & Woodward 1984) with generalization to non-ideal gas equation of state (Colella & Glaz 1985). This code solves the Euler equations, to which we add nuclear reactions and radiative diffusion through an operator-split formulation. The complete set of combustive Euler equations, including diffusive radiative transfer, can be written in state-vector form,

$$\frac{\partial \boldsymbol{Q}}{\partial t} + \nabla \cdot \boldsymbol{\Phi} = \boldsymbol{S}, \tag{6}$$

with the *state vector*

$$\boldsymbol{Q} \equiv \begin{bmatrix} \rho \\ \rho u \\ \rho E \\ \rho X_l \end{bmatrix}, \tag{7}$$

---

[3] See http://chandra.as.arizona.edu/~dave/tycho-intro.html.

the *flux vector*

$$\mathbf{\Phi} \equiv \begin{bmatrix} \rho \boldsymbol{u} \\ \rho \boldsymbol{uu} + p \\ (\rho E + p)\boldsymbol{u} + \boldsymbol{F}_r \\ \rho X_l \boldsymbol{u} \end{bmatrix}, \qquad (8)$$

and the *source vector*

$$\boldsymbol{S} \equiv \begin{bmatrix} 0 \\ \rho \boldsymbol{g} \\ \rho \boldsymbol{u} \cdot \boldsymbol{g} + \rho \epsilon_{\mathrm{net}} \\ R_l \end{bmatrix}, \qquad (9)$$

where $E = E_I + E_K$ is the total energy per gram, consisting of internal and kinetic energy components, and ρ, p, $\boldsymbol{u}$, $\boldsymbol{g}$, and T are the density, pressure, velocity, gravitational force field, and temperature, respectively. The net energy source term due to nuclear reactions and neutrino cooling is $\epsilon_{\mathrm{net}} = \epsilon_{\mathrm{burn}} + \epsilon_{\mathrm{cool}}$, and the time rate of change of composition X_l due to nuclear reactions is denoted R_l. The radiative flux is $\boldsymbol{F}_r = -k_r \nabla T$, with radiative "conductivity" $k_r = 4acT^3/(3\kappa_{\mathrm{R}}\rho)$ and Rosseland mean opacity κ_{R}. Self-gravity is implemented assuming that the interior mass at each radius is distributed with spherical symmetry. The mass interior to the inner boundary of the hydrodynamics grid is adopted from the TYCHO stellar model.

The stellar models, which are calculated on a finely meshed Lagrangian grid, are linearly interpolated onto the Eulerian hydrodynamics grid taking into account the subgrid representation of mass used in the PPM scheme. Mapping the models leads to small discrepancies in hydrostatic equilibrium. An equilibration to hydrostatic balance occurs through the excitation and then damping of low-amplitude, standing, predominantly radial pressure waves within the computational domain. These low-amplitude waves, which are well described by the linearized wave equation, have a negligible effect on the convective flow.

To save computational resources, we simulate carefully chosen subregions of the star. Thus, these calculations are local models of convection in the *box in a star* tradition. The advantage of local convection models is that higher effective resolution can be used than is currently possible in global circulation models. This approach, however, precludes investigation of the lowest order modes of flow, and we do not yet include rotation or magnetic fields, which are best studied using global domains. The boundary conditions used are periodic in angular directions and stress-free reflecting in the radial direction.

Our simulation code, dubbed PROMPI, has been adapted to parallel computing platforms using domain decomposition and the sharing of a three-zone layer of boundary values and uses the MPI message passing library to manage interprocess communication.

4. OXYGEN SHELL BURNING

We have evolved a 23 $M_\odot$ stellar model with the TYCHO code to a point where oxygen is burning in a shell that overlies a silicon-sulfur–rich core. Approximately 60% of the oxygen fuel available for fusion has been depleted at the time we begin the hydrodynamic simulation, when the star is $\sim 2 \times 10^6$ yr from the zero-age main sequence. Carbon-, helium-, and hydrogen-burning shells are also present contemporaneously at larger radii in the classic "onion skin" structure (Hoyle 1946). In one of the models presented here (ob.2d.e), which is also discussed in Meakin & Arnett (2006), we adopt an outer radius that encompasses both the oxygen- and carbon-burning shells. In this paper,

however, we restrict our analysis to the oxygen shell burning convection zone and the stable layers that bound it.

The oxygen shell burning model affords us the opportunity to study a thermally relaxed model because the thermal balance is determined by the very large neutrino cooling rates rather than the much lower radiative diffusion timescale (Arnett 1996, pp. 284–292). Neutrinos dominate the energy balance in the stable layers so that the stellar structure and the nature of convection are determined by the interplay between nuclear burning and neutrino emission (Aufderheide 1993; Arnett 1972). The effects of radiative diffusion are both unresolved and energetically unimportant during these evolutionary phases and have not been included in the oxygen shell calculations for computational efficiency.

The radial profile of the simulated region is presented in Figure 2. The temperature and density profiles betray the complex structure of the model, including the narrow burning shell that resides at the very base of the convection zone, which is coincident with the temperature peak. The initial extent of the convection zone can be identified by the plateau in oxygen mass fraction at $0.43 < r_9 < 0.72$ (where $r_9 = r/10^9$ cm). Characteristic of shell-burning regions, the entropy gradient is quite steep at the boundaries of the convection zone and gives rise to peaks in the buoyancy frequency at those locations. The initial location of the upper convective boundary is coincident with a small stable layer at $r \sim 0.72 \times 10^9$ cm, which is overwhelmed by the convective flow that develops in the simulation (see § 4.1). A new boundary forms where the stratification again becomes stabilizing at $r \gtrsim 0.8 \times 10^9$ cm. This mixing is shown in the change in ^{16}O abundance (Fig. 2, *top right panel*) after 400 s.

In Table 1 we list the 25 nuclei used in our network. This network reproduces to within 1% the energy generation of the full 177 element network used to evolve the 1D TYCHO model for the simulated conditions, including oxygen- and carbon-burning shells. During carbon burning the dominant reactions are ^{12}C(^{12}C, α)^{20}Ne and ^{12}C(^{12}C, p)^{23}Na, leaving an ash of ^{20}Ne, ^{23}Na, protons, and alpha particles. ^{20}Ne is photodisintegrated through the ^{20}Ne(γ, α)^{16}O reaction. The dominant reactions during oxygen burning are ^{16}O(^{16}O, α)^{28}Si, ^{16}O(^{16}O, p)^{31}P, and ^{16}O(^{16}O, n)^{31}S, leaving an ash of predominantly ^{28}Si and ^{32}S. Neglecting the nonalpha chain species ^{23}Na, ^{31}P and ^{31}S can affect the net energy generation rate during carbon and oxygen burning by a factor of a few under the conditions studied here. The reaction rates, including ^{12}C(α, γ)^{16}O, are from Rauscher & Thielemann (2000).

Nuclear evolution is time advanced using the same reaction network subroutines as the TYCHO code and uses implicit differencing (Arnett 1996). We include cooling by neutrino-antineutrino pair emission, denoted ϵ_{cool}, which results from photo, pair, plasma, bremsstrahlung and recombination processes (Beaudet et al. 1967; Itoh et al. 1996).

The Helmholtz equation-of-state code of Timmes & Swesty (2000) is used to represent the ion and electron pressure with an arbitrary degree of electron degeneracy. With our 25 nuclei network, the initial conditions are thermodynamically consistent with the initial TYCHO model to better than a few percent at all radii after mapping to the hydrodynamics grid.

We calculate oxygen shell burning models in 2D and 3D. Our baseline model, labeled ob.2d.c, is a 90° wedge embedded in the equatorial plane with radii encompassing the oxygen-burning convective shell and two stable bounding layers. The effects of dimensionality on the oxygen-burning convective shell are explored with a 3D model ob.3d.B, which has an angular extent of 27 deg^2. The influence of the upper boundary was studied with
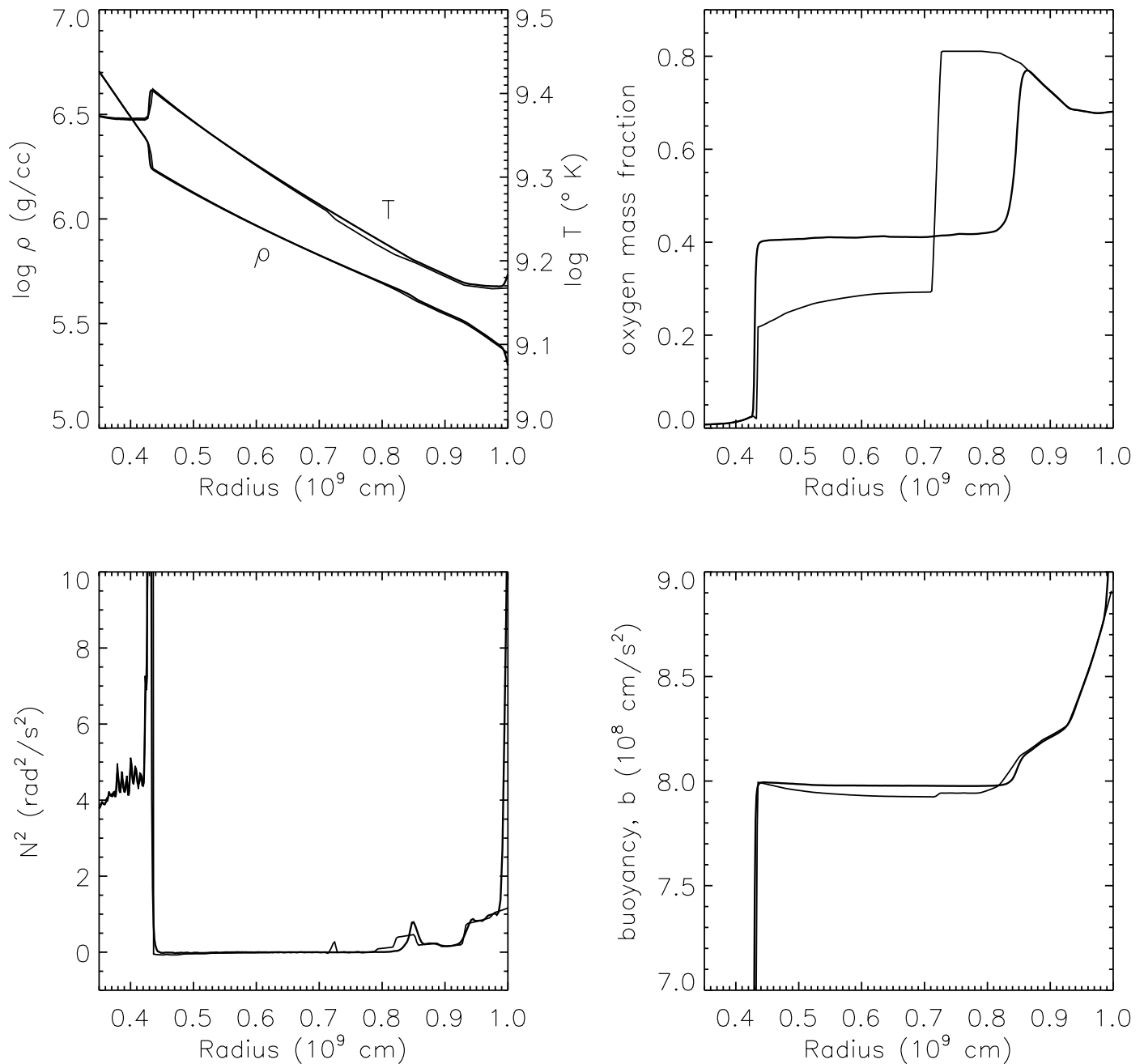
Fig. 2.—Radial profile of the simulated region for the oxygen shell burning models. The thin lines indicate the initial conditions, and the thick lines indicate the 3D model at $t = 400$ s. *Top left*: Temperature and density. *Top right*: Mass fraction of ^{16}O. *Bottom left*: Squared buoyancy frequency. *Bottom right*: Buoyancy.

model ob.2d.e, which includes the overlying carbon-burning convective shell as well (additional details concerning this model are presented in Meakin & Arnett 2006). A preliminary resolution study is undertaken with model ob.2d.C, which uses the same domain limits but twice the linear resolution of the baseline model. Properties of the oxygen shell burning models presented in this paper are summarized in Table 2.

4.1. *The Correct Mixing Boundary*

Convection is initiated through random low-amplitude (0.1%) perturbations in density and temperature applied to a region in the center of the convectively unstable layer on a zone-by-zone basis. (Two additional simulation models with the same characteristics as ob.2d.c were calculated that used perturbations with larger amplitudes [1%] and a low-order mode distribution. The

development of the convective flow was found to be insensitive to these differences.) The role played by the perturbations is to break the angular symmetry of the initial model and seed rising and sinking plumes whose growth is driven by nuclear burning, neutrino cooling, and the slightly superadiabatic background gradient imprinted in the initial TYCHO model. As the plumes rise, they penetrate the original convective boundary, which was determined in the TYCHO code using the Ledoux criterion. The initial evolution of the flow is presented in a time series of snapshots in Figure 3; the light yellow contour shows the initial outer convective boundary.

The location of the initial outer boundary can be seen as a small bump in the initial profile of the buoyancy frequency presented in Figure 2 at radius $r \sim 0.72 \times 10^9$ cm. The reason the boundary is stable in the 1D model but did not survive in the multidimensional

TABLE 1

NUCLEI INCLUDED IN REDUCED NUCLEAR REACTION NETWORK

Element	Charge	Atomic Weight
Helium................	2	4
Carbon................	6	12
Oxygen................	8	16
Neon...................	10	20
Sodium................	11	23
Magnesium...........	12	24
Silicon	14	28
Phosphorus...........	15	31
Sulfur.................	16	32, 34
Chlorine..............	17	35
Argon	18	36, 38
Potassium	19	39
Calcium...............	20	40, 42
Titanium..............	22	44, 46
Chromium	24	48, 50
Iron...................	26	52, 54
Nickel.................	28	56

NOTE.—Network also includes electrons, protons, and neutrons.

TABLE 2

SUMMARY OF OXYGEN SHELL BURNING MODELS

Parameter	ob.3d.B	ob.2d.c	ob.2d.C	ob.2d.e
$r_{\rm in}$, $r_{\rm out}$ (10^9 cm)...............	0.3, 1.0	0.3, 1.0	0.3, 1.0	0.3, 5.0
$\Delta\theta$, $\Delta\phi$ (deg).....................	30, 30	90, 0	90, 0	90, 0
Grid zoning	$400 \times (100)^2$	400×320	800×640	800×320
$t_{\max}$ (s)...............................	800	574	450	2,400
$v_{\rm conv}$ (10^7 cm s^{-1})	0.8	2.0	1.8	1.8
$t_{\rm conv}$ (s)	103	40	44	44
$\dot{M}_i\|_u$[a] (10^{-4} $M_\odot$ s^{-1})	1.1	1.33	1.25	1.3
$\dot{M}_i\|_l$[a] (10^{-4} $M_\odot$ s^{-1})..........	−0.23	−0.52	−0.5	−0.5

[a] The subscripts u and l refer to the upper and lower convective shell boundary, respectively.

simulation is because of the local nature of the Ledoux criterion used. This can be appreciated by the fact that although the buoyancy frequency at this location is positive, and hence locally stable to convective turnover, the *buoyancy jump* across this region is very small, $\Delta b \sim 3 \times 10^6$ cm s^{-2}, compared to the turbulent kinetic energy in the adjacent flow, by which it is easily overwhelmed. This type of inconsistency can be relatively easily removed from 1D simulations by using a parameter akin to the bulk Richardson number (eq. [2]) to characterize convective boundaries in place of the Ledoux or Schwarzschild criteria. For the original outer boundary Ri$_B \lesssim 1$, a condition under which a boundary is expected to mix on an advection timescale, akin to the expansion of turbulence into a homogenous medium.

The relationship between Ri$_B$ and the traditional Schwarzschild and Ledoux criteria can be elucidated by writing the buoyancy frequency in terms of the well-known "nablas" used in stellar evolution,

$$N^2 = \frac{g\beta_T}{H_P} \left(\nabla_{\rm ad} - \nabla_s + \frac{\varphi}{\beta_T} \nabla_\mu \right), \qquad (10)$$

where $\nabla = (d \ln T / d \ln p)$, ∇_s is the gradient of the stellar background, $\nabla_{\rm ad}$ is the gradient due to an adiabatic displacement, $\nabla_\mu = (d \ln \mu / d \ln p)$ is the mean molecular weight gradient, and the thermodynamic derivatives are $\beta_T = -(d \ln \rho / d \ln T)$ and $\varphi = (d \ln \rho / d \ln \mu)$. Therefore, the Ledoux criterion is simply

$$N^2 > 0. \qquad (11)$$

The Schwarzschild criterion is the same, but with the stabilizing effect of the mean molecular weight gradient ∇_μ neglected. For comparison, the bulk Richardson number can be written as Ri$_B \sim N^2 hL/\sigma^2$, where h is some measure of the boundary width. A convective boundary will start to become stabilizing when

$$N^2 \gtrsim \sigma^2/(hL). \qquad (12)$$

This criterion is based on a finite threshold for stability that takes into account the strength of the convective turbulence. In addition, the bulk Richardson number is more than a simple stability criterion; it is also an indicator of the rate at which boundary

erosion will proceed. We conclude that the correct criterion for determining the extent of a convective zone is neither the Ledoux nor the Schwarzschild criterion, which are both static, linear, and local criteria, but a *dynamic boundary condition*, based on the bulk Richardson number, which we discuss in more detail in § 7.

4.2. *Time Evolution*

The rich dynamics taking place at the convective boundary is apparent in the time evolution of the 3D flow presented in Figure 4, which provides a global view of the evolution. The top panel shows the evolution in time and radius of the oxygen abundance gradient, represented by a color map in which light is large and dark is small. At the beginning of the simulation (*far left*) the colors are smooth as the turbulence has not yet developed. The light line near the bottom of the panel is the lower boundary of the convective shell, where oxygen is separated from the silicon-sulfur core below. The short horizontal band at $r \sim 0.72 \times 10^9$ cm is the initial weakly stable convective boundary discussed above; it is overwhelmed in the first 100 s by convection. After $\sim$300 s the abundance distribution has approached a quasi–steady state, with slow growth of the convective region. The bottom of the convection zone moves downward, but at a much slower rate than the upper boundary moves outward. The mottled appearance in the convection zone is due to the ingestion of new oxygen entrained from above, followed by turbulent mixing. At the top boundary of the convection zone an oscillatory behavior can be seen, and in the overlying stable region wave motions are apparent.

The bottom panel in Figure 4 shows the radial profile of the kinetic energy, which illustrates a major feature of the convection: intermittency. While these simulations are well described by a statistical steady state over a few convective turnover times, at any instant the fluctuations are significant. The flow is episodic, with bursts of activity followed by lulls. The bursts in kinetic energy in the convection zone are seen to induce wave trains in both the upper and lower stable layers. Characteristic of g-modes, the phase velocity (orientation of the wave crests) is orthogonal to the group velocity (direction of energy transport) in these wave trains, which can be seen by comparing the composition and kinetic energy profiles.

4.3. *Quasi-steady Oxygen Shell Burning Convection*

Following the transient readjustment of the outer boundary, the oxygen-burning convective shell attains a quasi-steady character. In Figure 5 we present the time evolution of the integrated internal, gravitational, and kinetic energy. The energy is calculated by forming horizontal averages of the flow properties and then
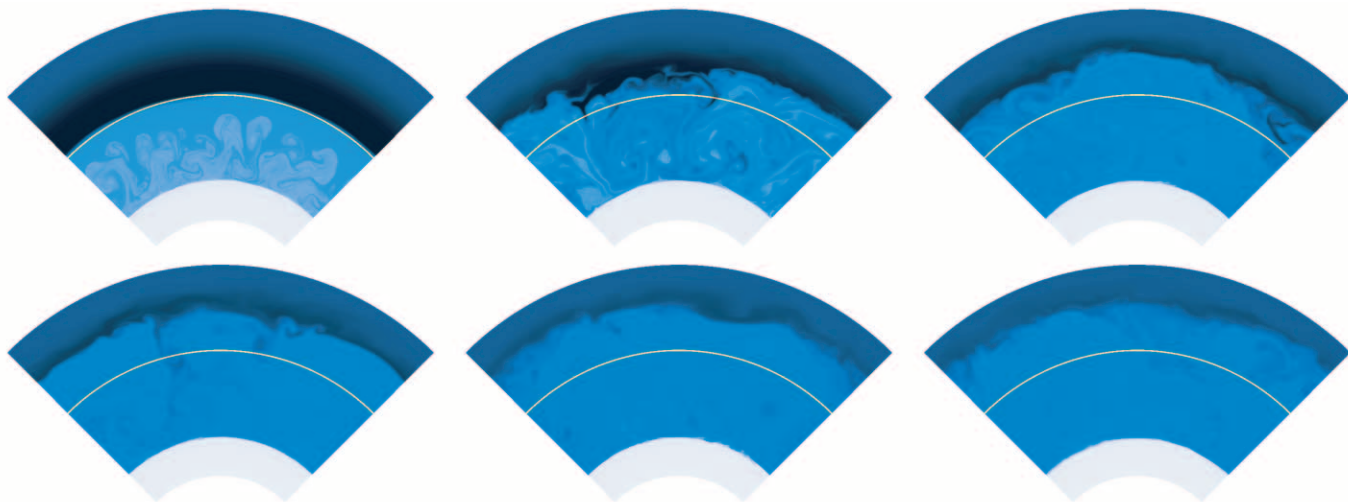
Fig. 3.—Time sequence showing the onset of convection in the oxygen shell burning model. The first 200 s of the 2D model (ob.2d.c) is shown, including the initial transient and the settling down to a new quasi–steady state. The light yellow line indicates the location of the convective boundary as defined in the 1D TYCHO stellar evolution model (Ledoux criterion), which was used as initial conditions for the simulation.

assuming a full spherical geometry. The gravitational energy contribution from material on the computational grid is calculated according to

$$E_G \equiv \int \frac{GM(r)\,dM}{r}\,dr, \qquad (13)$$
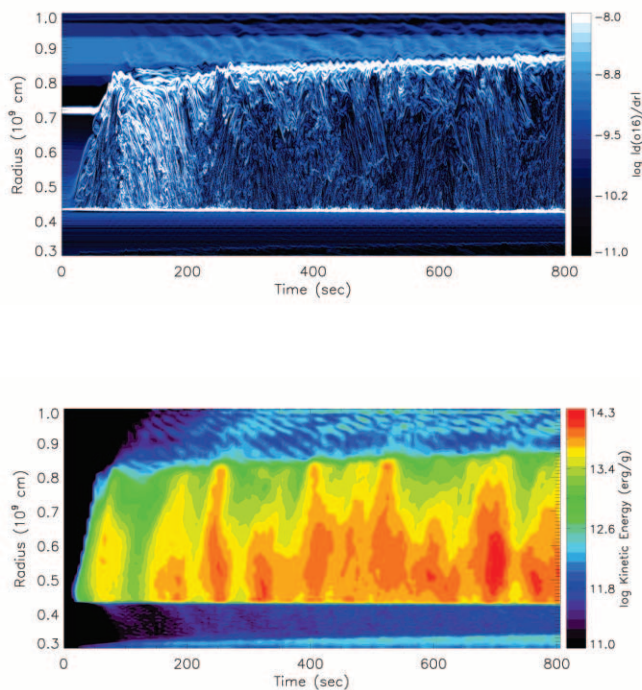
Fig. 4.—Time evolution of the 3D oxygen shell burning model. *Top*: Magnitude of the oxygen abundance gradient is shown and illustrates the migration of the convective boundaries into the surrounding stable layers. Interfacial oscillations are also apparent in the upper convective boundary layer ($r \sim 0.85 \times 10^9$ cm), and internal wave motions can be seen quite clearly in the upper stable layer. *Bottom*: Kinetic energy density is shown and illustrates the intermittent nature of the convective motions. The upwelling chimney-like features in the convective region are seen to excite internal wave trains in the stable layers, which propagate away from the boundaries of the convection zones. See also Fig. 25.

where the mass increment is $dM = 4\pi r^2 \langle \rho \rangle$ and the integral is taken over the radial limits of the grid.

The total kinetic energy levels off in all of the models by $t \sim 300$ s. The 2D models are characterized by a much larger overall kinetic energy. The total kinetic energy settles down to a slow increase as the oxygen shell evolves; this is true for both 2D and 3D.

The radial profiles of the rms velocity fluctuations are presented in Figure 6 for the 2D and 3D models. The velocity fluctuation amplitudes in all of the 2D models are higher than the 3D model by a factor of ~ 2. The 2D models also assume a significantly different radial profile than the 3D model and a flow structure that is dominated by large convective vortices that span the depth of the convection zone. The signature of these large eddies is apparent in the horizontal velocity components, as well as the fairly symmetric shape of the radial velocity profile within the convection zone. The velocity components in the 3D model reveal an upflowing and downflowing circulation with horizontal deflection taking place in a fairly narrow layer at the convective boundaries.

Although significant differences exist between 2D and 3D models, the 2D models are found to be in good agreement with each other to the extent that the statistics have converged, which are calculated over the time period $t \in [300, 450]$ s. The time period for calculating statistics was limited by the model ob.2d.C, which was only run as far as $t \sim 450$ s. The agreement among the 2D models shows that the outer boundary condition (tested by model ob.2d.e) and the grid resolution (tested by model ob.2d.C) are not playing a decisive role in determining the overall structure of the flow, at least in these preliminary tests. The agreement in overall velocity amplitude in the upper stable layer in model ob.2d.e indicates that the stable layer velocity amplitudes are not strongly affected by the details of the modes that are excited in that region. This gives credence to the analysis in Meakin & Arnett (2007), which assumes that the stable layer velocity amplitudes are determined by the dynamical balance between the convective ram pressure and the wave-induced fluctuations.

The convective turnover times $t_c = 2\Delta R / v_{\mathrm{conv}}$ for the 2D models are all of order $t_c \sim 40$ s, and they span between 10 and 55 convective turnovers. The turnover time for the 3D model is $t_c \sim 100$ s, and the model spans approximately eight convective turnovers.
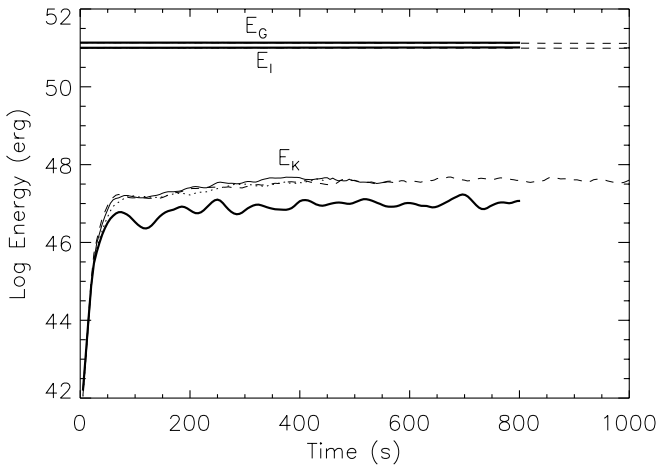
FIG. 5.—Time evolution of the energy budgets for the oxygen shell burning models: the 3D model (*thick line*) and the three 2D models (*thin lines*) are shown, including ob.2d.c (*thin solid line*), ob.2d.e (*thin dashed line*), and ob.2d.C (*thin dotted line*). The energy budget includes the internal energy E_I, the gravitational energy E_G, and the kinetic energy E_K. Note that the energy scale is logarithmic, so that the 3D kinetic energy is much smaller than the 2D values.

The radial profiles of the net enthalpy flux carried by the 2D and 3D convective flows are found to be in good agreement with each other and with the 1D TYCHO model, despite the differences in the morphology and velocity amplitudes of the flow. In the 2D models, it is found that although the *net* enthalpy flux is consistent with the 3D model, the fluxes in the up- and down-welling flows are significantly larger than in the 3D model. This can be explained by a lower turbulent mixing efficiency in the 2D simulations, a property of the 2D flows that is also indicated by the significantly larger composition inhomogeneities that arise and persist during boundary layer entrainment events (Meakin & Arnett 2007).

4.4. *Stable Layer Dynamics during Shell Burning*

In both the 2D and 3D models, the stably stratified layers are characterized by velocity fluctuations throughout their extents (Fig. 6). These fluctuations are the signature of g-modes that are excited by the convective motions. In the 2D model, the amplitudes of the stable layer velocity fluctuations are higher. In the lower stable layer, the 2D models also have a much smaller ratio

of horizontal to radial velocity amplitude. The velocity amplitude ratio is roughly proportional to the ratio of the mode frequency and buoyancy frequency, $v_r/v_\perp \approx \omega/N$ (Press 1981), so that the waves excited in the 2D model are of lower frequency. The velocity ratios in the upper stable layer are comparable between the 2D and 3D models, although the 2D amplitudes are higher by a factor of ~ 2.

During late burning stages, multiple concentric convective shells form that are separated by stably stratified layers. These intervening stable layers act as resonating cavities for g-modes that are excited by the turbulent convection. In Meakin & Arnett (2006) it was shown that the stable layer motions in model ob.2d.e can be decomposed into individual g-modes that are well described by the linearized nonradial wave equation (Unno et al. 1989). Meakin & Arnett (2007) showed that a good estimate for the amplitudes of the wave motions (and the associated thermodynamic fluctuations) in both the 2D and 3D models can be made by assuming that the pressure fluctuations associated with the g-modes balance the ram pressure of the turbulent convection. In the latter paper, a single mode (frequency and horizontal scale) was assumed, based on integral properties of the turbulence (convective turnover time and mixing-length scale). In this section we present the spectrum of motions present in the stable layers and turbulent regions for the more realistic 3D model.

For a given background structure, a spectrum of eigenmodes exist that are solutions to the nonradial wave equation and boundary conditions. Individual modes can be uniquely identified by a horizontal wavenumber index l and oscillation frequency ω. In Figure 7, l-ω diagrams are presented for the convection zone and the two bounding stable layers. The individual l-ω components have been isolated through Fourier transforms of a time sequence of the simulation data.

Several modal components or "branches" can be identified in the stable layer diagrams (*left and right panels*). These include (1) p-modes, seen as a series of points at the lowest l-values that extend to high frequencies; (2) g-modes, which appear as ridges that are bound above by the buoyancy frequency; and (3) f-modes, which appear as a ridge separating the g- and p-modes. The f-modes are interfacial waves and are most prominently seen in the lower boundary diagram at a radius $r = 0.4 \times 10^9$ cm. The f-mode signature is due to interfacial waves running along the convective boundary at $r \sim 0.43 \times 10^9$ cm, where there is a spike in buoyancy frequency.
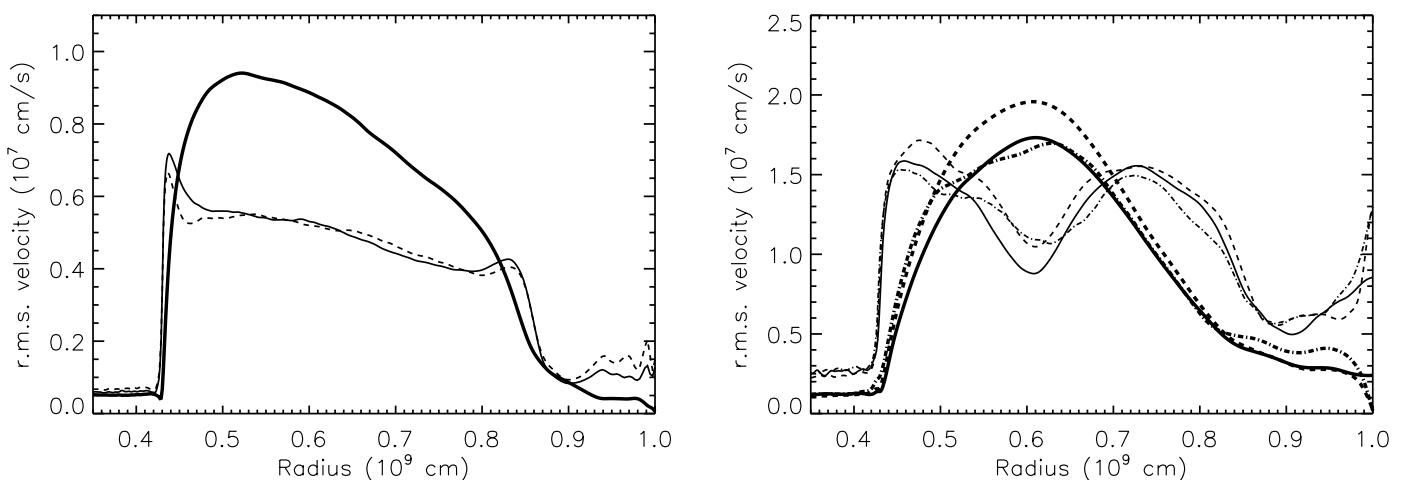

FIG. 6.—The rms velocity fluctuations for oxygen shell burning. *Left*: 3D model, with velocity components v_r (*thick solid line*), v_θ (*thin solid line*), and v_ϕ (*thin dashed line*). *Right*: 2D models, with velocity components v_r (*thick line*) and v_ϕ (*thin line*) for simulations ob.2d.e (*solid line*), ob.2d.c (*dashed line*), and ob.2d.C (*dot-dashed line*).
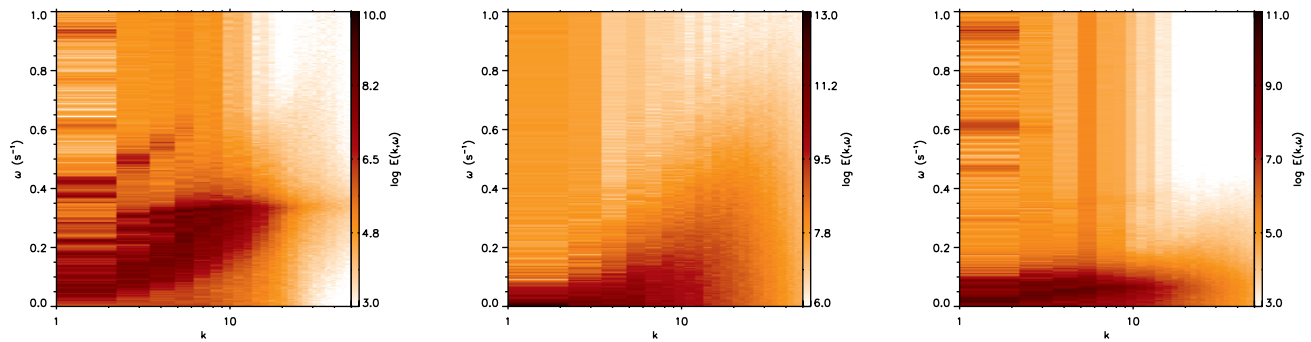
FIG. 7.—Mode diagrams for several radial positions in the oxygen shell burning model showing the dominant spatial scales and timescales on which motions occur. The abscissa measures k, which is related to the wavenumber index l of the mode by $l = 12k$. The three locations shown here include the following: lower stable layer, just beneath the convective shell $r = 0.4 \times 10^9$ cm (*left*); middle of convective shell, $r = 0.6 \times 10^9$ (*middle*); and upper stable layer, just above the convective shell $r = 0.9 \times 10^9$ cm (*right*).

In the convection zone, the spectrum is dominated by power at low temporal and spatial frequencies. This strong nonmodal convection signature is also present, although at lower amplitude, in the stable layers. This "turbulence" spectrum extends from the lower left corner of the diagrams and is similar to that seen in the simulations of He shell burning by Herwig et al. (2006).

5. CORE CONVECTION

Are the hydrodynamic features of oxygen shell burning of more general applicability? To investigate this, we examined core convection during hydrogen burning. Because of the long thermal timescale for radiative diffusion in such stars, we focus on the hydrodynamic behavior of a model in which the inner boundary provides a driving luminosity about 10 times larger than natural. This allows us to simulate the convection with our compressible hydrodynamics code; an anelastic method (if multifluid) would allow this to be done in the star's natural timescale. While our calculation is not thermally relaxed on a Helmholtz-Kelvin timescale, it does relax dynamically and provides some clue as to the convective behavior.

We have previously evolved a 23 $M_\odot$ star onto the main sequence with TYCHO, to an age of 2.4×10^5 yr, at which point hydrogen is burning in a convective core. The model is then mapped onto the PROMPI hydrodynamics grid for simulation. This model represents an early point in main-sequence evolution, in which the core hydrogen content has been depleted by only 1.7% ($X_{core} = 0.689$, $X_{init} = 0.701$, $\Delta X = 0.012$). The inner radius of the simulation was chosen such that the convectively unstable region covers ~1 pressure scale height (convective cores are usually only of order a pressure scale height because of the divergence of the scale height toward the stellar center). The entire domain covers ~5 pressure scale heights and ~3.3 density scale heights. The density contrast across the computational domain is ~30 with a contrast of ~2 across the convectively unstable region.

The radial profile of the simulated region is presented in Figure 8, including the run of temperature, density, composition, buoyancy frequency, and relative buoyancy. The entropy jump at the edge of the convective core, due to the fuel-ash separation, gives rise to a buoyancy jump (spike in buoyancy frequency).

The equation of state for the main-sequence model is well described by an ideal gas with radiation pressure component. The ratio of gas to total pressure lies in the range $0.85 < \beta < 0.95$, with an increasing contribution from radiation pressure as the stellar center is approached. A single composition representing

hydrogen has been evolved to keep track of nuclear transmutation and the mean molecular weight of the plasma. A metallicity of $Z = 0.01879$ has been used to represent the additional 175 species in the initial TYCHO model, and helium is calculated according to $Y = 1 - (X + Z)$, where X is the self-consistently evolved hydrogen mass fraction.

The luminosity due to nuclear burning in the computational domain is a small fraction of the total stellar luminosity (2.4%), which is dominated by burning in the inner regions of the core and $L_{tot} = 7.8 \times 10^4 L_\odot$. Core burning is incorporated into the simulation as an input luminosity at the inner boundary of the computational domain.

The Kelvin-Helmholtz timescale for this model is $t_{K-H} \sim 10^5$ yr, which is many orders of magnitude longer than the dynamical timescales that are feasible to simulate. In addition, the small luminosity of the star produces a convective velocity scale that is very subsonic ($M \sim 10^{-3}$). Since we are not interested in the thermal relaxation of the model, we have boosted the input luminosity by a factor of 10 to increase the velocity scale of the flow. This was necessary because our fully compressible code is limited by the sound crossing time.

Radiation transport is treated in the diffusion limit. Opacities are approximated by Thomson scattering, which agrees well with the OPAL opacities (Iglesias & Rogers 1996) used in the 1D TYCHO model for the region simulated. The effects of radiative diffusion, however, are found to be unresolved in the current simulation (with the diffusion time across a single zone $\tau_{rad} = \Delta^2/k_{rad} \gg t_{conv}$, with grid zone size Δ), and therefore energy transport in the convection zone occurs primarily on the subgrid level due to numerical diffusion. This is a high Péclet number simulation.

A 2D model and a 3D model have been calculated. The simulated wedges have angular extents of $30°$ in both the polar and azimuthal directions and are centered on the equator to avoid zone convergence problems near the poles. This minimal angular domain size was chosen by calculating models of increasing angular size in 2D domains until the flow pattern converged. The angular domain size used in the present simulations encompasses a large convective roll in 2D. Smaller 2D domains were found to distort the convective roll, while domains larger by integer multiples contained proportionally more rolls of the same flow amplitude and morphology. The boundary conditions in the radial direction are reflecting and stress-free, and periodic conditions are used in both angular directions. The grid zoning, domain limits, and simulation run times are summarized in Table 3 for the 2D and 3D models.
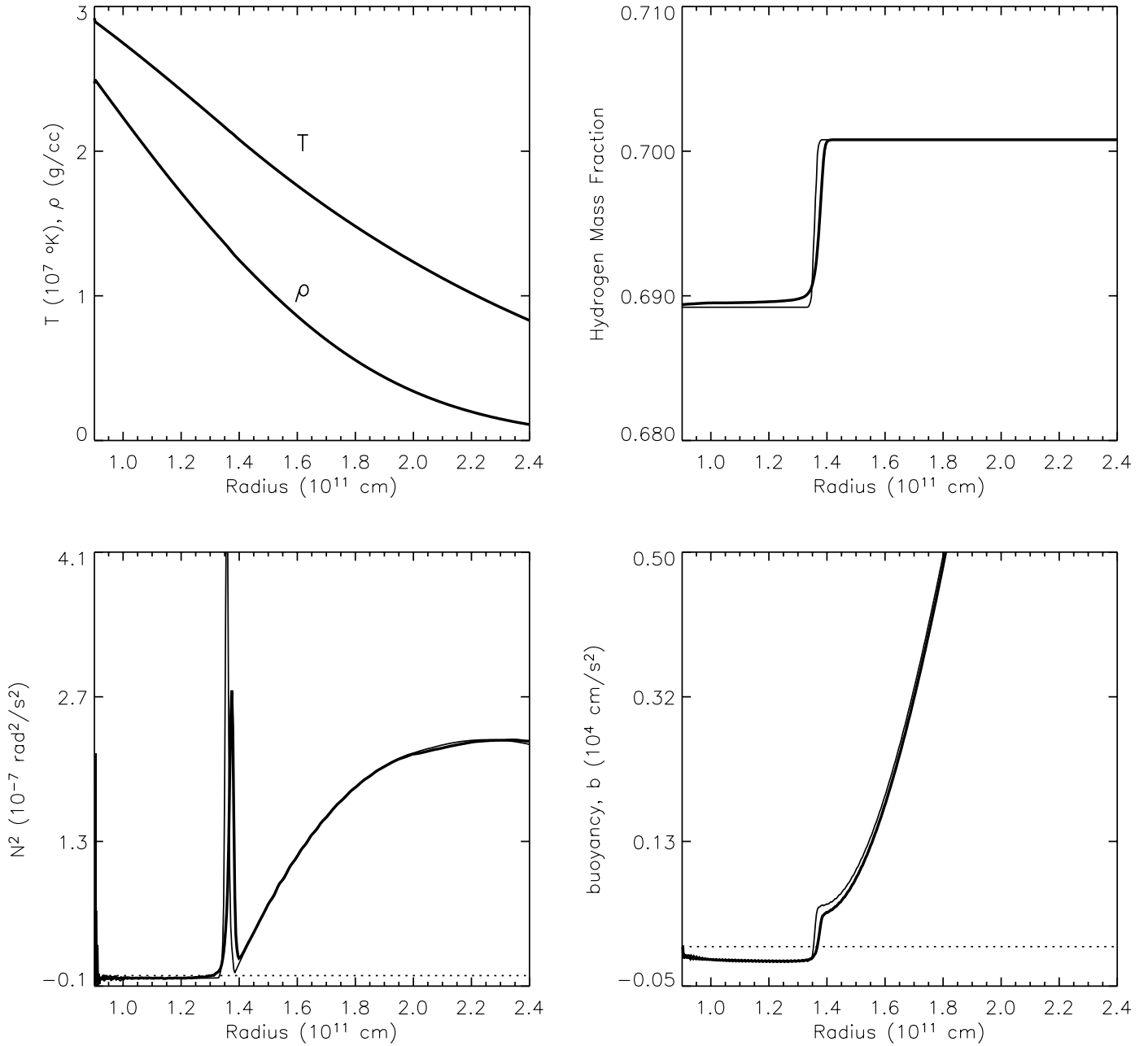
FIG. 8.—Radial profile of the simulated region for the main-sequence core convection model. The thin lines show the initial conditions, and the thick lines show the state of the 3D model at $t = 10^6$ s. *Top left*: Temperature and density. *Top right*: Hydrogen abundance. *Bottom left*: Squared buoyancy frequency. *Bottom right*: Buoyancy.

5.1. Quasi-steady Core Convection

Convection is initiated through random low-amplitude (0.1%) perturbations in density and temperature applied as in the oxygen shell simulation. In order to save computing time, the 3D model was initiated on a domain one-quarter as large in azimuthal angle, which was then tiled 4 times in angle once convective plumes began to form. The initial development of the flow in the 3D model is presented in Figure 9 as a time sequence of velocity isosurfaces. The turbulent structure of the convective flow, as well as the excitation of internal waves that radiate into the overlying stably stratified layer, is clearly illustrated. A comparison of the flow morphology between the 2D and 3D models is presented in Figure 10. The 2D convective flow is much more organized and laminar and is dominated by a single large convective cell, while the 3D convection is composed of many smaller scale plumelike

TABLE 3
SUMMARY OF "CORE CONVECTION" MODELS

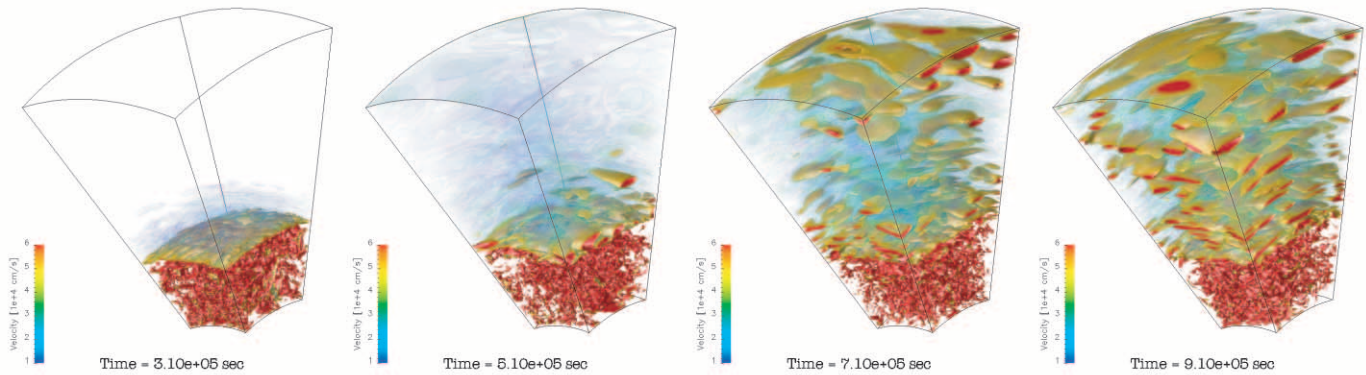| Parameter	msc.3d.B	msc.2d.b
r_{in}, r_{out} (10^{11} cm)	0.9, 2.5	0.9, 2.5
$\Delta\theta$, $\Delta\phi$ (deg)........................	30, 30	30,0
Grid zoning............................	$400 \times (100)^2$	400×100
t_{max} (s)......................................	2.0×10^6	2.0×10^6
v_{conv} (10^5 cm s^{-1})..................	2.5	13
t_{conv} (s)	3.6×10^5	6×10^4
$\dot{M}_i$ (10^{-7} $M_\odot$ s^{-1})	2.72	4.73

FIG. 9.—Velocity isocontours showing the development of the flow in the 3D core convection model. The turbulent convective flow excites internal waves that radiate into the overlying stably stratified layer. By the end of the time sequence shown the stable layer cavity is filled with resonant modes.

structures and is more obviously turbulent. In both models the stably stratified regions are rife with internal waves excited by the convection.

The 3D convective flow attains a quasi-steady character after approximately 6×10^5 s, or approximately two convective turnovers. The evolution of the internal, gravitational, and total kinetic energy components on the computational grid for the 2D and 3D models is presented in Figure 11 and is calculated in the same way as for the oxygen-burning model. In both the 2D and 3D models, the total kinetic energy fluctuates in times with excursions from the mean as large as $\delta E_K / \overline{E_K} \sim 0.4$ in 3D and $\delta E_K / \overline{E_K} \sim 0.6$ in 2D. The kinetic energy in the 2D model grows on a slightly longer timescale and achieves a steady character after $\sim 10^6$ s, at which time the kinetic energy growth rate tapers off. The total energy is conserved to better than $\sim 0.2\%$ for both the 2D and 3D flows by the end of the calculation.

The rms velocity fluctuations are presented in Figure 12 for the 2D and 3D models. The resultant flows in both the 2D and 3D models are similar to that found for the oxygen shell burning model. The velocity amplitudes are higher in 2D by a factor of ~ 5 (see axis scale in Figure 12), and the flows are dominated by large eddies spanning the depth of the convective region. The horizontal deflection of matter is also found to occur in a much narrower region in the 3D model. The hard-wall lower boundary of the 3D model is characterized by an even narrower horizontal flow, probably due to the absence of a stable layer that can host the horizontal flows associated with g-modes.

The time-averaged convective flow velocity for the 3D model is $v_c \approx 2.8 \times 10^5$ cm s^{-1}. The turnover time is $t_c = 2\Delta R / v_c \approx 3.2 \times 10^5$ s, and the simulation spans approximately five convective turnovers. The peak velocity fluctuation is $v_{\text{peak}} \sim 2 \times 10^6$ cm s^{-1}, corresponding to a peak Mach number of $M \sim 0.03$, and the maximum density fluctuations within the convective flow are $\sim 0.02\%$, which is of order M^2 as expected for low Mach number thermal convection (Gough 1969). The time-averaged convective flow velocity in the 2D model is $v_c \approx 1.3 \times 10^6$ cm s^{-1}, and the convective turnover time for this model is $t_c \approx 7 \times 10^4$ s. The simulation spans 1.5×10^6 s, which is ~ 21 convective turnovers. The peak velocity fluctuation in the 2D model is comparable to that in the 3D simulation, with $v_{\text{peak}} \sim 2 \times 10^6$ cm s^{-1}, and the peak density fluctuation is a little more than twice that found in the 3D model, $\sim 0.05\%$. The turnover times and convective velocity scales are summarized in Table 3.

5.2. *The Stable Layer Dynamics Overlying the Convective Core*

As in the oxygen shell burning model, the stably stratified layers in the core convection models are characterized by velocity fluctuations throughout. Similar to shell burning, the 2D stable layer velocity amplitudes are larger and have a smaller radial-to-horizontal component ratio $v_r / v_\perp \approx \omega / N$ compared to the 3D flow. The dependence of the wave spectrum on dimensionality seen in our suite of models suggests that one should be cautious when drawing conclusions from 2D simulations of wave-turbulence interactions, particularly when the turbulence
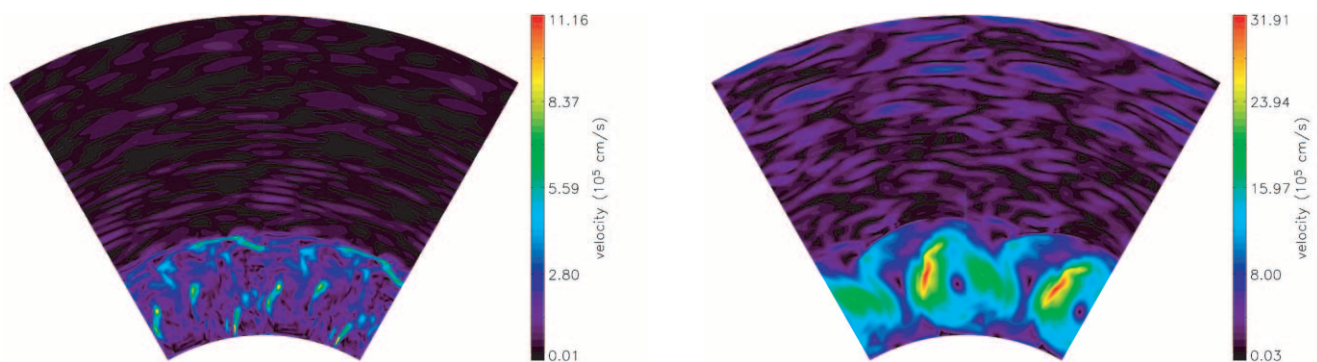

FIG. 10.—Velocity magnitude for the core convection model at $t = 10^6$ s: a slice through the 3D model (*left*) and the 2D model (*right*). The topology of the convective flow is significantly different between 2D and 3D models: the 3D convective flow is dominated by small plumes and eddies, while the 2D flow is much more laminar and dominated by large vortical eddies that span the depth of the layer. The wave motions in the stable layer have similar morphology in 2D and 3D, but the velocity amplitudes are much larger in 2D. The computational domains have been tiled once in angle for presentation.
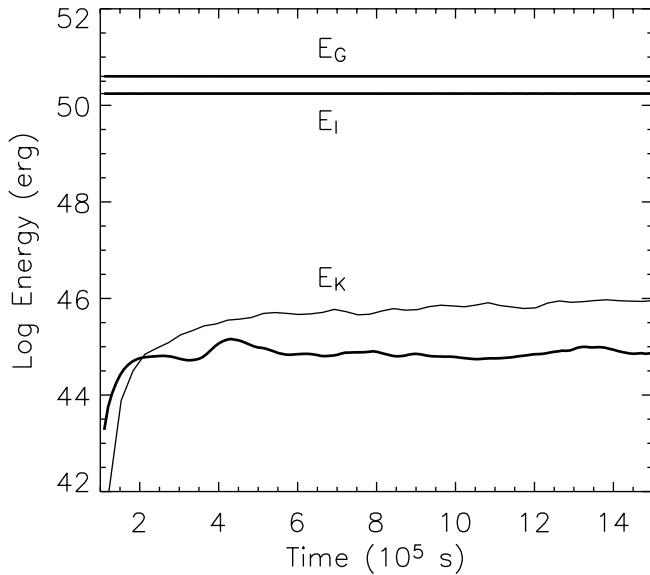
Fig. 11.—Time evolution of the energy budget for the main-sequence core convection models: the 3D model (*thick line*) and the 2D model (*thin line*) are shown. The energy budget includes the total internal energy E_I, gravitational energy E_G, and kinetic energy E_K on the computational grid.

is driven at a significantly higher than natural rate (e.g., Rogers & Glatzmaier 2005a, 2005b).

The stable layer motions in the core convection simulation are predominantly resonant modes, which compare well to the analytic eigenmodes of the linearized wave equation, and are analogous to those discussed for the oxygen shell burning model. The region outside the convective core will act as a resonant cavity, with the outer boundary at the location where the buoyancy frequency and Lamb frequency cross (Unno et al. 1989).

The amplitudes of the internal waves excited will be determined by the ram pressure of the turbulence at the convective boundary. In Figure 13 the ram pressure and horizontal rms pressure fluctuations are presented for the 3D model and can be seen to balance at the interface between the convective core and the

stably stratified layer. Using this condition of pressure balance, Meakin & Arnett (2007) estimate the amplitudes of the excited internal wave velocities and the induced thermodynamic fluctuations and find this to be in good agreement with the oxygen shell burning simulations. The relationship between the density fluctuations, the convective velocity scale, and the stellar structure (i.e., N and g) was found to be

$$\frac{\rho'}{\langle\rho\rangle} \sim M_c^2 + \frac{v_c N}{g}. \qquad (14)$$

That this proportionality holds in the core convection model as well, where fluctuation amplitudes are lower than those in the oxygen shell burning model by an order of magnitude, is illustrated in Figure 14, which presents the buoyancy frequency and density fluctuation profiles for the boundary region. The density fluctuations in the simulation and the value calculated according to equation (14) compare remarkably well, with $\rho'/\langle\rho\rangle \sim 0.12\%$.

6. SIMULATIONS AND MIXING-LENGTH THEORY

In this section we compare our 3D oxygen shell burning simulation results to the MLT of convection. We choose to compare this particular simulation since it represents the most physically complete model in our suite of calculations, in terms of both dimensionality and thermal evolution. Unless otherwise specified, the time period over which averaging is performed on the simulation data is $t \in [400, 800]$ s, which is approximately four convective turnovers. We find that this period is sufficiently long compared to the time evolution of the flow that average values are not affected appreciably by increases in the averaging time period.

6.1. *Mixing-Length Theory Picture*

The physical picture underlying the MLT, which is the standard treatment of convection used in 1D stellar evolution modeling (see Cox & Giuli 1968; Clayton 1983; Kippenhahn & Weigert 1990; Hansen & Kawaler 1994), is one in which large eddies are accelerated by an unstable temperature gradient, advect a certain distance, and then suddenly lose their identity through turbulent mixing with the *background*. Energy is transported through this
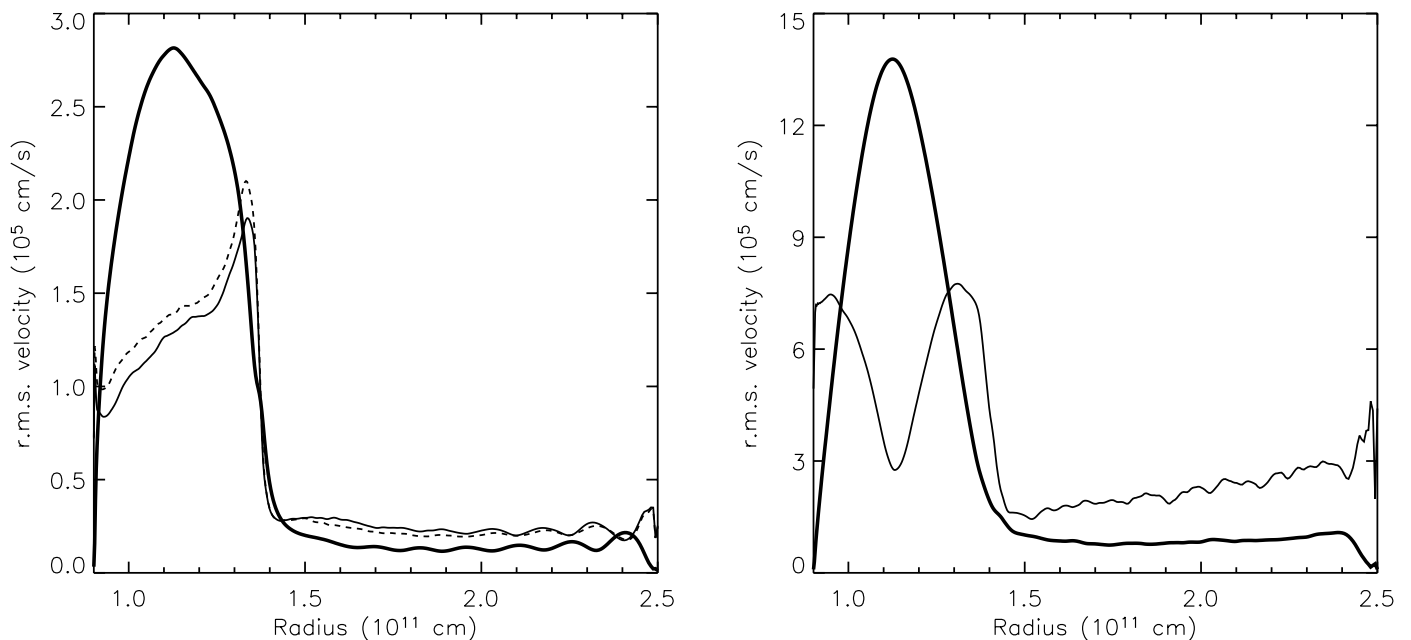

Fig. 12.—The rms velocity fluctuations for the core convection model: the 3D model (*left*) and the 2D model (*right*). In each plot, the thick line indicates the radial velocity component and the thin line is used to indicate horizontal velocity components, with the dashed line used to show the polar angle component in the 3D model.
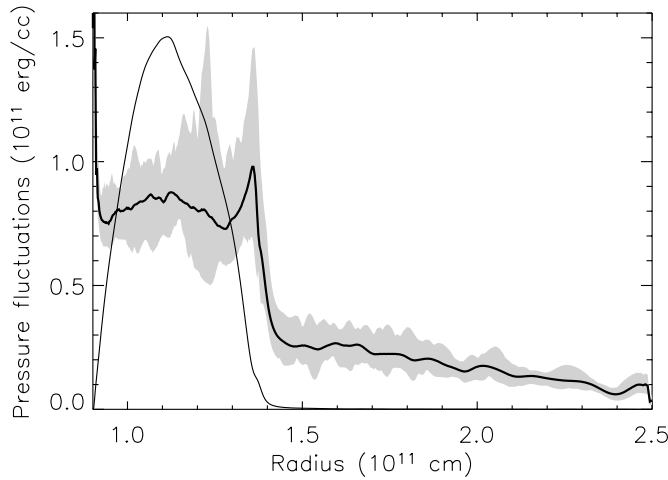
FIG. 13.—Pressure fluctuations in core convection model. The time-averaged horizontal rms pressure fluctuations are shown as the thick line, with extreme values over two convective turnovers indicated by the shaded region. The thin line shows the radial component of the turbulent ram pressure ρv_r^2 averaged over a convective turnover. At the upper boundary, the lines cross at a point where the turbulent pressure is balanced by the wave-induced pressure fluctuations in the stable layer. This crossing point is coincident with the location of the convective boundary. The pressure perturbations at the lower boundary are due to the input luminosity that drives the convective flow.

process because the *blobs* that are accelerated radially outward have a higher entropy at their formation location than where they *dissolve*. The vertical distance over which these large eddies retain their identity is a fundamental parameter in the MLT. This *mixing length* Λ is generally taken to be a multiple of the local pressure scale height $\Lambda = \alpha_\Lambda H_p$.

Within this physical picture, the MLT develops a relationship between the convective flux, the temperature gradient, the large eddy velocity scale, and the geometrical factors that describe the large-scale eddies. The starting point in MLT is the expression for the radial enthalpy flux. In terms of the turbulent fluctuations it is taken to be (assuming a horizontally isobaric flow)

$$F_c = v_c \rho c_P T'. \quad (15)$$
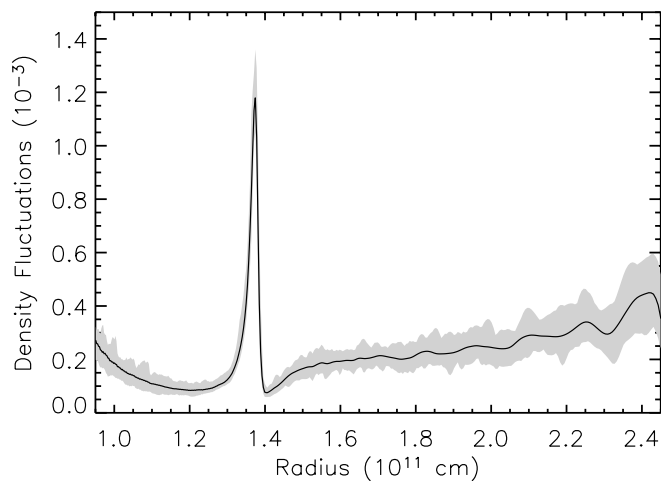
The temperature fluctuations in MLT are related to the temperature gradient and the distance traveled by the large eddy by

$$T'/T = \left(\frac{\partial \ln T_e}{\partial r} - \frac{d \ln T_0}{dr} \right) \frac{\Lambda}{2} = (\Delta \nabla) \frac{1}{H_p} \frac{\Lambda}{2}, \quad (16)$$

where the subscript "e" indicates properties of the large eddies and the unsubscripted temperature gradient is that of the appropriately averaged background stratification. The dimensionless temperature gradient ∇ is used here (see § 4.1), and the difference between the change in the eddy temperature as it moves vertically and the averaged stellar background is written as

$$\Delta \nabla = (\nabla - \nabla_e).$$

The factor of $\frac{1}{2}$ in equation (16) represents the idea that on average the large convective eddies have traversed about half a mixing length before reaching the current position.

The velocity obtained by the convective eddy is computed by calculating the work done by the buoyancy force over a mixing length,

$$v_c^2 = g\beta_T(\Delta \nabla) \frac{\Lambda^2}{8H_p}. \quad (17)$$

Here again, the eddy is assumed to have been accelerated over half of a mixing length and an additional factor of $\frac{1}{2}$ is incorporated on the right-hand side to account for energy lost driving other flows, such as small-scale turbulence and horizontal motions (e.g., note that the rms horizontal velocity is of the same order as the rms radial velocity in the simulation).

The average convective flux can then be written as

$$F_c = \rho c_p T \sqrt{g\beta_T} \frac{\Lambda^2}{4\sqrt{2}H_p^{3/2}} (\Delta \nabla)^{3/2}. \quad (18)$$

The temperature gradient for the convecting material is found by assuming that eddies follow isentropic trajectories $\nabla_e = \nabla_{\rm ad}$. Deviations from isentropic motion have been considered in the MLT. In the case of strong radiative diffusion losses, the eddy
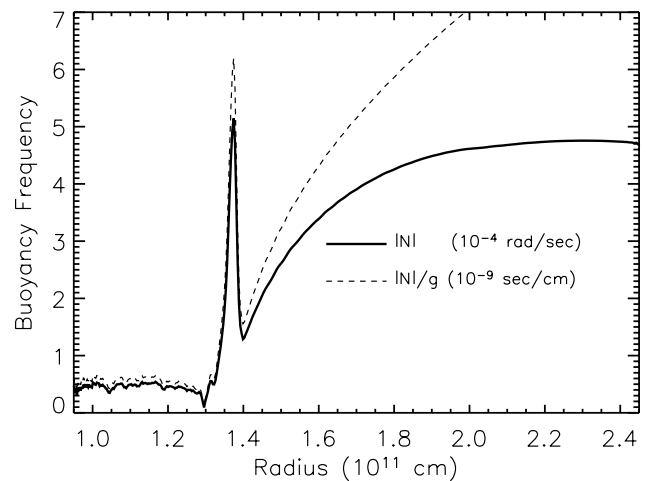

FIG. 14.—*Left*: Density fluctuations in the 3D core convection model. The time-averaged maximum density fluctuation is shown as the thick line, with extreme values for the averaging period (two convective turnovers) shown by the shaded region. The largest fluctuations occur at the interface between the turbulent convective region and the stably stratified layer. The maximum fluctuation at the interface is $\rho'/\langle\rho\rangle \sim 0.12\%$. *Right*: The buoyancy frequency is shown in units of 10^{-4} rad s^{-1}. Also shown by the dashed line is the buoyancy frequency normalized by the gravity that sets the scale of the density fluctuations at the convective boundary through eq. (14). The expected density fluctuation is $\rho'/\langle\rho\rangle \sim v_c|N|/g \sim 0.12\%$, where a velocity scale of $v_c \sim 2 \times 10^5$ cm s^{-1} has been used (see Fig. 12).
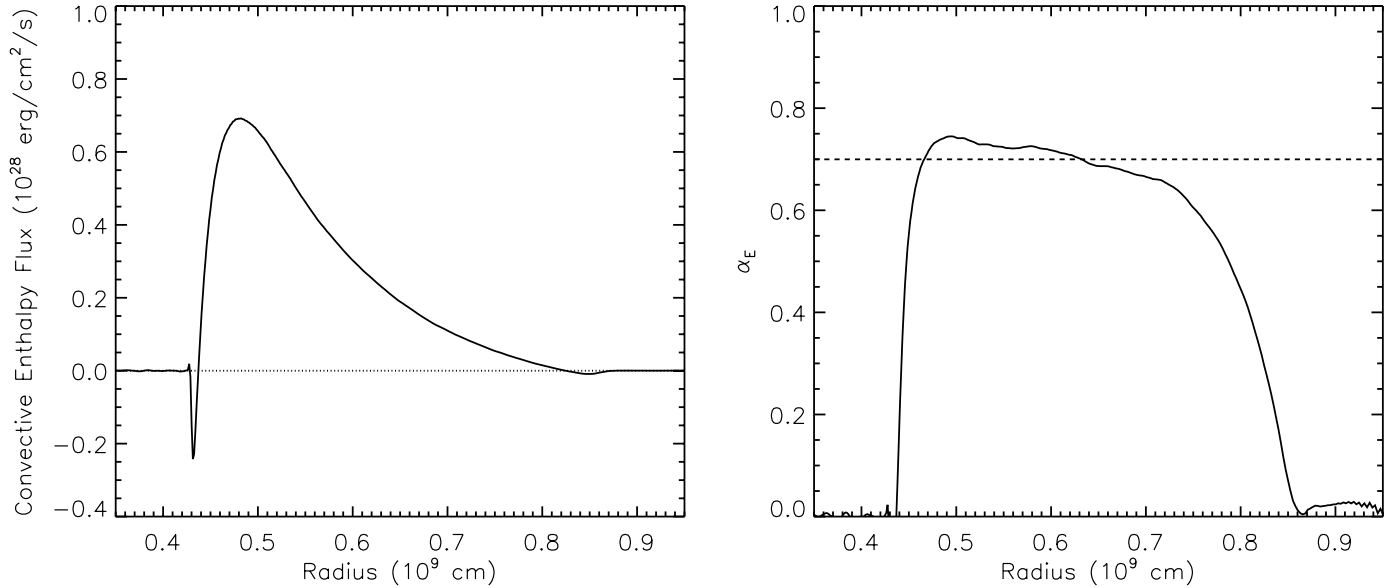
Fig. 15.—*Left*: Convective enthalpy flux, $F_c = \overline{\langle \rho c_p v_r T' \rangle}$. *Right*: Temperature-velocity correlation function α_E calculated according to eq. (22), with mean value $\langle \alpha_E \rangle = 0.7$ shown by the dashed line.

geometry (in terms of the surface area–to–volume ratio) is an important additional parameter as the eddies are envisioned to *leak* a fraction of their thermal energy over a mixing-length distance. When local cooling dominates, through either radiative losses (in optically thin regions) or neutrino losses (such as in the present model), the geometry of the eddies is not important since energy escapes everywhere from the large eddies, not just at eddy "surfaces."

During the oxygen shell burning simulations being considered here, nonadiabatic losses are small over a convective turnover time and the convection is expected to be "efficient." A quantitative measure of convective efficiency is the Péclet number, which is the ratio of the energy-loss timescale to the convective turnover timescale for the large eddies. In the current model, energy losses are dominated by neutrino cooling ϵ_ν. Therefore, we calculate an effective Péclet number using the following convective and neutrino-cooling timescales:

$$\tau_c \sim \frac{H_p}{v_c}, \qquad (19)$$

$$\tau_\nu \sim \frac{c_p T'}{T' \partial \epsilon_\nu / \partial T} = \frac{c_p T}{\epsilon_\nu} \left(\frac{\partial \ln \epsilon_\nu}{\partial \ln T} \right)^{-1}, \qquad (20)$$

$$\mathrm{Pe} = \frac{\tau_\nu}{\tau_c} \sim \frac{v_c c_p T}{H_p \dot{\epsilon}_\nu} \left(\frac{\partial \ln \epsilon_\nu}{\partial \ln T} \right)^{-1} \sim 10^4 \left(\frac{\partial \ln \epsilon_\nu}{\partial \ln T} \right)^{-1}, \qquad (21)$$

where characteristic values from the simulation have been used in equation (21), and the temperature dependence of the neutrino loss rates is $(\partial \ln \epsilon_\nu / \partial \ln T) \lesssim 9$. Therefore, the Péclet number for the convection is $\mathrm{Pe} \gtrsim 10^3$, and we should expect the convection zone to be very nearly isentropic.

6.2. *The Enthalpy Flux, Background Stratification, and Temperature and Velocity Fluctuations*

The convective enthalpy flux measured in the simulation is presented in Figure 15. The negative values of the flux at the bottom and the top of the convective shell reflect the braking of the convective flows at these boundaries. The enthalpy flux is calculated by performing time and horizontal averages on the flow.

MLT assumes that the velocity and temperature fluctuations are perfectly correlated, so that horizontal averaging of fluctuations is comparable to products of the averages. To test the degree to which the velocity and temperature fluctuations are correlated, we calculate the coefficient, α_E, defined in the following way:

$$F_c = \langle \rho c_p T' v_c' \rangle = \alpha_E \langle \rho c_p \rangle \langle T' \rangle \langle v_c' \rangle. \qquad (22)$$

In computing α_E, the fluctuations T' and v_c' in equation (22) are taken to the be the rms fluctuations in the horizontal plane in the simulation. The radial profile of α_E is shown in Figure 15. We find $\langle \alpha_E \rangle = 0.7 \pm 0.03$ averaged over the radial interval $r \in [0.5, 0.75] \times 10^9$ cm within the convection zone. A value of α_E smaller than unity indicates that the horizontal distributions of temperature and velocity fluctuations are not perfectly correlated. The degree of correlation, however, is fairly uniform throughout the convection zone.

In order to assess the validity of the MLT temperature and velocity fluctuation amplitudes given by equations (16) and (17), we calculate the correlation coefficients α_T and α_v, which are defined by

$$T'/T = (\Delta \nabla) \alpha_T \qquad (23)$$

and

$$v_c = \frac{\alpha_v}{2} \sqrt{g \beta_T (\Delta \nabla) H_p}. \qquad (24)$$

In Figure 16 the temperature gradient of the horizontally averaged hydrodynamic model profile ∇_{sim}, as well as the adiabatic ∇_{ad} and the composition-corrected (Ledoux) gradient $\nabla_{\mathrm{Led}} = \nabla_{\mathrm{ad}} + (\varphi/\beta_T)\nabla_\mu$, are presented.

The superadiabatic temperature profile of the stellar background $\Delta \nabla = \nabla_{\mathrm{sim}} - \nabla_{\mathrm{ad}}$ is presented in the right panel of Figure 16. While the convection zone is found to have a superadiabatic profile throughout, it is very small ($\Delta \nabla \lesssim 10^{-3}$). This confirms the efficiency of the convection, in accord with our estimate for Pe. Stability is maintained in the upper boundary layer by the composition gradient, where we have $\nabla_{\mathrm{ad}} < \nabla_{\mathrm{sim}} < \nabla_{\mathrm{Led}}$.
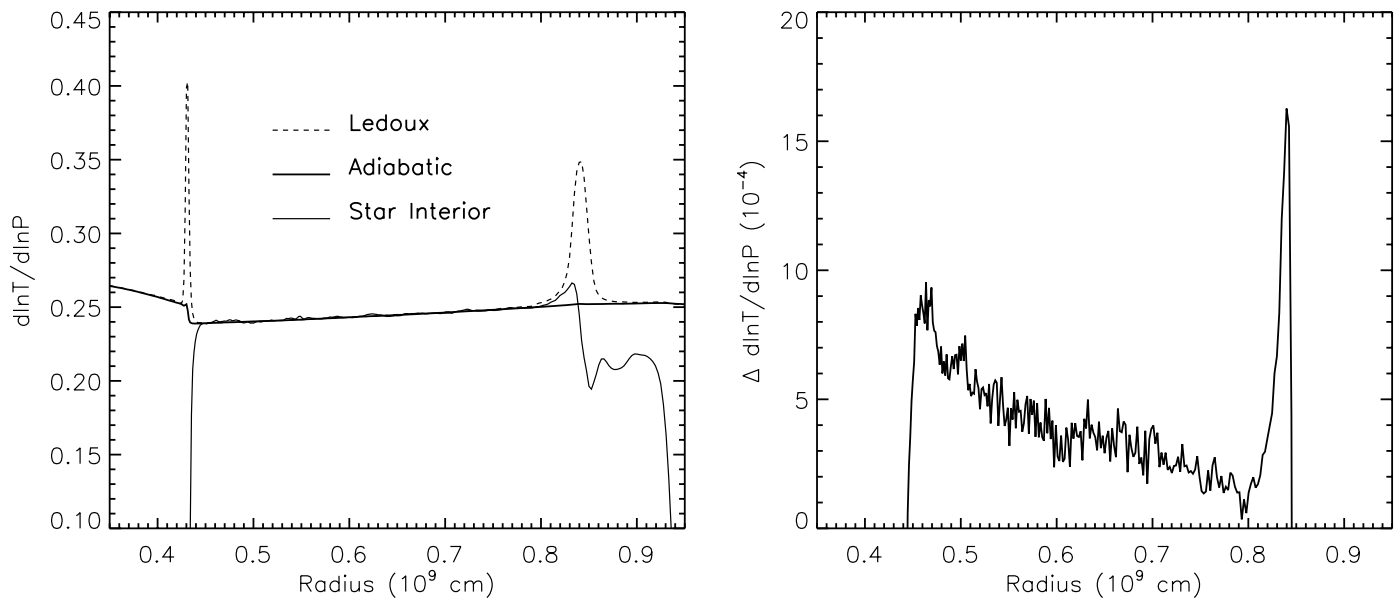
Fig. 16.—*Left*: Dimensionless temperature gradients: the stellar interior ∇_{sim}, adiabatic ∇_{ad}, and Ledoux ∇_{Led} gradients are shown. *Right*: Superadiabatic temperature gradient ($\nabla_{sim} - \nabla_{ad}$) horizontally and time averaged.

A question of practical concern is how to measure the temperature and velocity fluctuations T' and v_c in the simulations for comparison to MLT. In the MLT, these fluctuations are identified with the properties of large eddies. Therefore, a direct comparison would entail isolating the large eddies within a complex flow and measuring their properties. In lieu of a more complicated procedure, we identify the fluctuations in the large eddies using the following two distinct quantities for comparison: (1) the rms fluctuations relative to the horizontal mean, and (2) the mean fluctuation relative to the horizontal average considering the upflowing and downflowing material separately.

The temperature fluctuations calculated using these two methods are presented in Figure 17. The temperature fluctuations in

the convection zone follow a trend similar to the superadiabatic gradient, i.e., decreasing with increasing radius. In the right panel of Figure 17 the radial profile of α_T is shown using both definitions of the fluctuations. The nonzero temperature fluctuations outside the convective region are due to distortions in stable layers due to convective buoyancy braking (Meakin & Arnett 2007); the use of separate upflows and downflows is cleaner, eliminating these. The slopes in the temperature fluctuation profiles are slightly overcompensated for by the superadiabatic gradient when forming the ratio α_T. Within the scatter, however, α_T is fairly well represented by a constant value. The mean value within the body of the convection zone (taken to be $r \in [0.5, 0.75] \times 10^9$ cm) is larger for the rms fluctuations $\langle \alpha_T(rms) \rangle = 0.73$ compared to
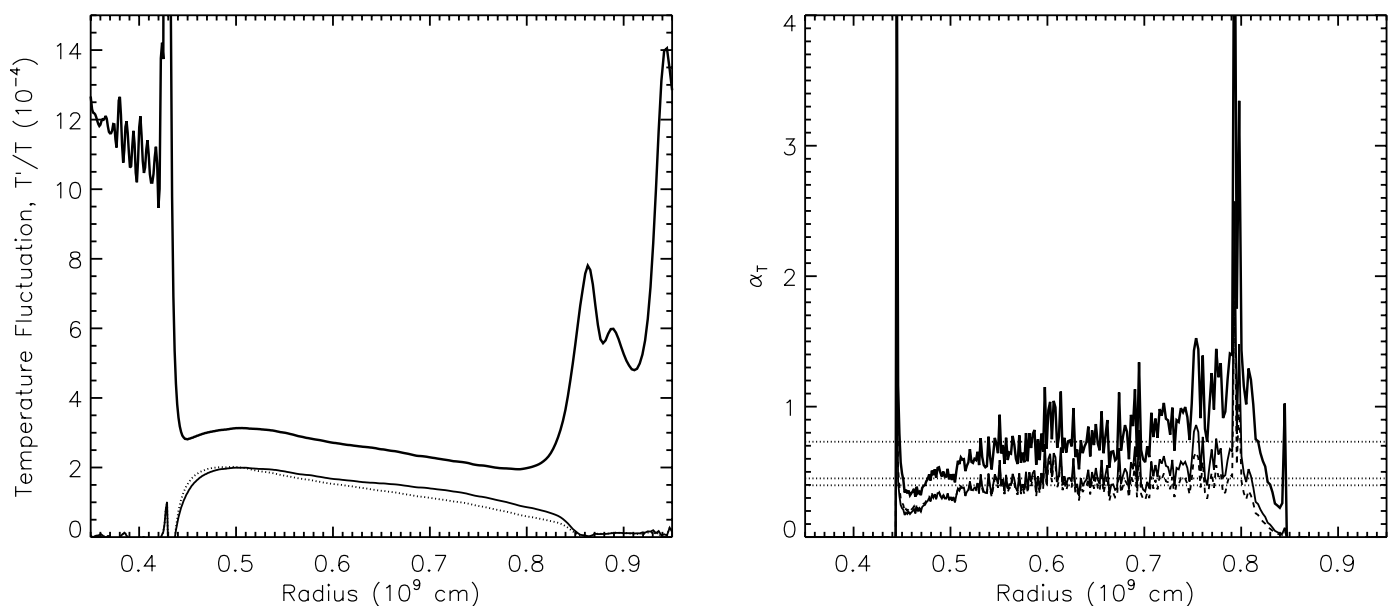

Fig. 17.—*Left*: Time-averaged rms temperature fluctuations: the thick solid line shows the rms fluctuations; the thin solid and thin dotted lines show the fluctuations in the upward- and downward-directed flow components, respectively. *Right*: Radial dependence of the "thermal mixing-length" parameters α_T defined by eq. (23) shown using the temperature fluctuations presented in the left panel, using the same line types. The mean values, averaged over $r \in [0.5, 0.75] \times 10^9$ cm, are shown by the thin dotted lines.
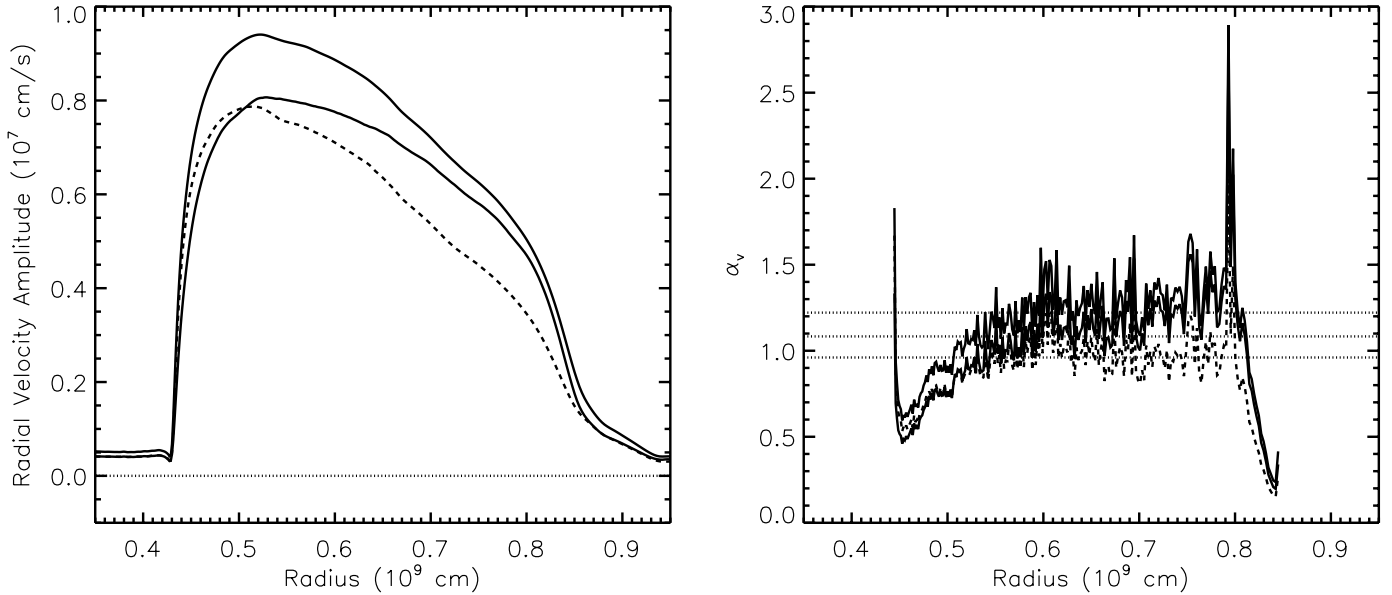
FIG. 18.—*Left*: Radial velocity amplitudes: rms value (*thick solid line*) and the mean upflow and downflow velocities (*thin solid and thin dashed lines, respectively*). *Right*: Radial dependence of the "velocity mixing-length" parameters α_v defined by eq. (24) shown for the velocity amplitudes presented in the left panel, using the same line types. The mean values, averaged over $r \in [0.5, 0.75] \times 10^9$ cm, are shown by the thin dotted lines.

$\langle \alpha_T(\text{up}) \rangle = 0.45$ and $\langle \alpha_T(\text{down}) \rangle = 0.40$. In all cases the correlation departs most from the mean value at the base of the convection zone, $r \lesssim 0.52 \times 10^9$ cm, where the nuclear flame is driving the convective flow.

The corresponding analysis for the velocity fluctuations is presented in Figure 18. The overall trends are similar for α_T and α_v. The mean values of α_v within the body of the convection zone are $\langle \alpha_v(\text{rms}) \rangle = 1.22$, $\langle \alpha_v(\text{up}) \rangle = 1.08$, and $\langle \alpha_v(\text{down}) \rangle = 0.96$. The largest departure from constancy is again found to be at the base of the convection zone (the flame region).

The sharp decrease in the effective mixing length near the lower boundary is not entirely surprising. The distance to the convective boundary provides an upper limit to the mixing length, while farther away from the boundaries the mixing length is limited by the distance over which eddies can maintain their coherence. This effect is possibly more exaggerated at the lower boundary because of the steep gradient in velocity that is needed to move the energy out of the burning zone. In contrast, the upper boundary is characterized by a more gentle deceleration of material and a "softer" boundary (i.e., lower N^2). Ignoring this boundary effect and using the same mixing-length parameter throughout the convection zone would result in a shallower temperature gradient near the boundary. The stiff temperature dependence of the nuclear reaction rates may therefore be affected.

The absolute calibrations of α_T and α_v are somewhat arbitrary and are scaled by factors of order unity for a particular formulation of the MLT based on the heuristic arguments discussed in § 6.1. According to equations (16), (17), (23), and (24), the equivalencies are $\alpha_{\Lambda,T} = 2\alpha_T$ and $\alpha_{\Lambda,v} = \sqrt{2}\alpha_v$, where the values subscripted by Λ indicate the MLT values defined by Kippenhahn & Weigert (1990). The corresponding values for the simulation are $\langle \alpha_{\Lambda,v}(\text{rms}) \rangle = 1.73$, $\langle \alpha_{\Lambda,v}(\text{up}) \rangle = 1.53$, and $\langle \alpha_{\Lambda,v}(\text{down}) \rangle = 1.35$ for velocity fluctuations and $\langle \alpha_{\Lambda,T}(\text{rms}) \rangle = 1.46$, $\langle \alpha_{\Lambda,T}(\text{up}) \rangle = 0.9$, and $\langle \alpha_{\Lambda,T}(\text{down}) \rangle = 0.8$ for temperature fluctuations.

The ratio $\alpha_{\Lambda,T}/\alpha_{\Lambda,v}$ is 0.84, 0.59, and 0.60 using the rms, upflow, and downflow values, respectively. In relation to the present simulation, a higher degree of consistency (i.e., $\alpha_{\Lambda,v} = \alpha_{\Lambda,T}$) can

be brought to this formulation of the MLT by scaling the velocity fluctuation in equation (17) by the inverse of the ratio $\alpha_{\Lambda,T}/\alpha_{\Lambda,v}$. Physically, this translates into a higher efficiency (by a factor of ~ 1.2–1.7) for the buoyancy work to accelerate the large eddies over the value $\frac{1}{2}$ adopted above, which is reasonable considering the heuristic argument used. Alternatively, agreement can be made by scaling the temperature fluctuations in equation (16) by the same ratio, which amounts to decreasing the distance over which eddies remain coherent and adiabatic as they move across the convection zone. Both of the these effects are plausible, as well as a combination of the two so long as the ratio is maintained. Which is operating in the present simulation? Unfortunately, the degeneracy between these two parameters cannot be broken because they combine linearly when calculating the enthalpy flux, which therefore does not provide a further constraint. Finally, *it is possible that the effective mixing lengths for temperature and velocity fluctuations are different*, a notion that is supported by the correlation lengths that we discuss next.

6.3. Correlation Length Scales

In the top panels of Figure 19 the vertical correlation length scales, calculated according to equation (B1), are presented for the velocity and temperature fluctuations. The vertical scale height is defined as the FWHM of the correlation function and can be written in terms of the correlation length in the positive and negative directions, $L_V = L_V^+ - L_V^-$. The relative values of L_V^+ and L_V^- give an indication of asymmetries in the eddies (Fig. 19, *bottom left panel*): $L_V^+/L_V^- = 1$ is a symmetric eddy, $L_V^+/L_V^- > 1$ is an eddy flattened on the bottom, and $L_V^+/L_V^- < 1$ is an eddy flattened at the top. Based on this simple diagnostic, both the temperature and velocity correlations indicate that the eddies near the lower boundary are flattened on the bottom, and those at the upper boundary are flattened on the top. The "overshooting" distance ($h \sim 10^7$ cm at the upper boundary and $h \lesssim 10^6$ cm at the lower boundary; see § 7.1), which is best described as an elastic response to the incoming turbulent elements, is very small compared to the correlation lengths measured here. Therefore, these eddies are effectively hitting a "hard wall" on reaching the boundaries.
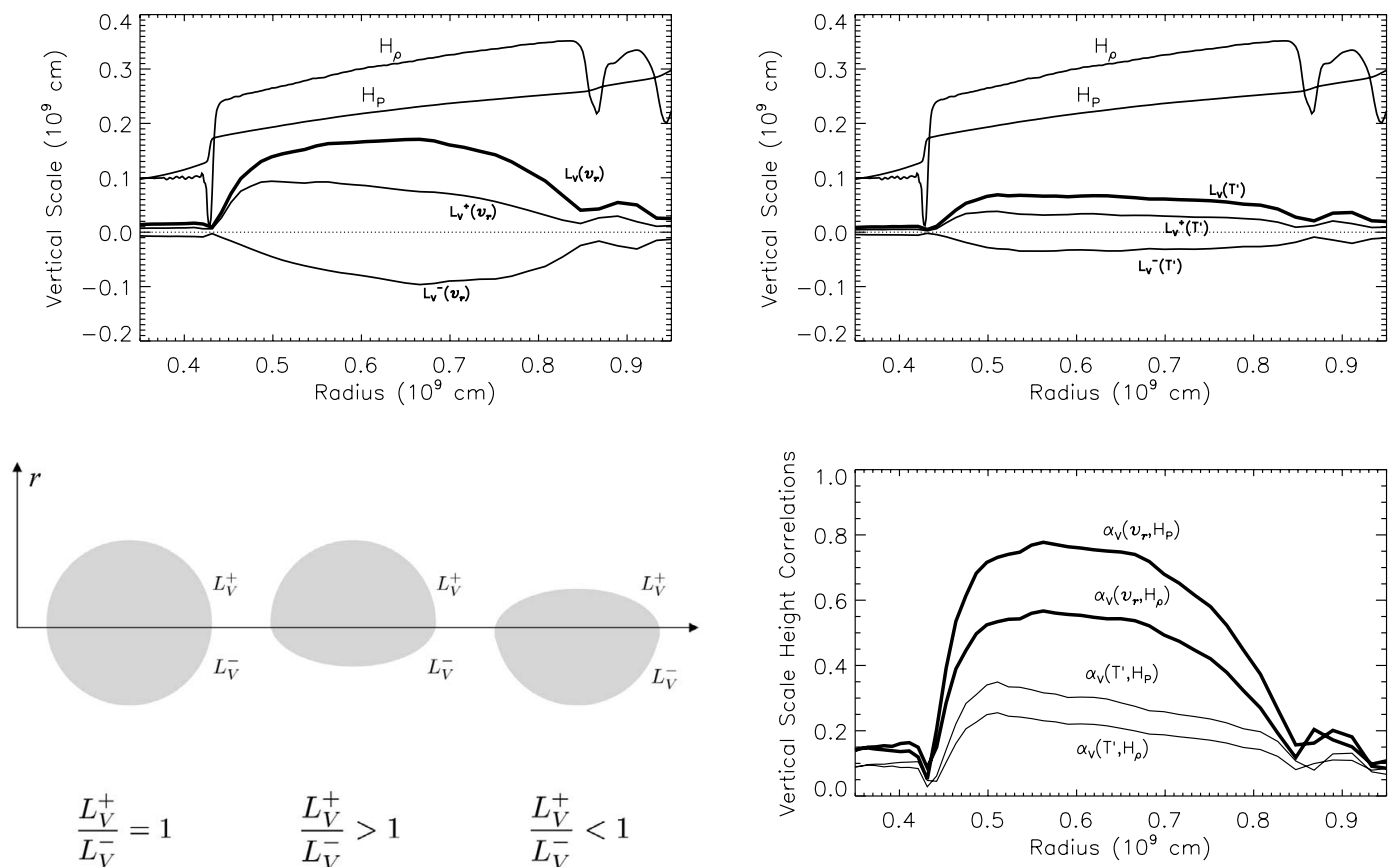
Fig. 19.—Vertical correlation length scales L_V as defined in Appendix B. *Top left*: L_V for velocity fluctuations, v'_r. *Top right*: L_V for temperature fluctuations, T'. The pressure scale height H_p and density scale height H_ρ are shown for comparison. *Bottom left*: Illustration of the relationship between eddy shape and the correlation length scales, L_V^+ and L_V^-. The gray patches represent the shapes of the eddies, and the $L_V^{+/-}$ values are measured in the radial direction, away from the horizontal line. *Bottom right*: Correlation lengths L_V scaled to pressure and density scale heights, e.g., $\alpha_V(v_r, H_p) = L_V(v_r)/H_p$.

The signature of this eddy "flattening" is also present in the radial profile of the full width length scale, L_V. In the case of velocity, which has larger correlation lengths, significant asymmetries are present throughout the convection zone. The smaller length scales associated with the temperature fluctuations permit a broad region throughout the convection zone where the eddies are roughly symmetric ($L_V^+/L_V^- \approx 1$) and appear to be uninfluenced by the boundaries. In this intermediate region, away from the boundaries, the temperature fluctuation length scales are relatively constant in size, even decreasing with radius, in contrast to the pressure and density scale heights, which are increasing with radius.

In the standard MLT, the convective eddies are assumed to be comparable in size to the mixing length. How do the correlation length scales compare to the mixing-length parameters found above? The bottom left panel of Figure 19 shows the ratios of L_V to the pressure and density scale heights. None of these curves are particularly constant within the convection zone, and boundary effects are particularly strong throughout the convection zone in the case of the velocity correlations. Interestingly, the velocity correlation parameter $\alpha_v(v_r, H_p) = L_V(v_r)/H_p$ is larger than the temperature correlation parameter $\alpha_v(T', H_p) = L_V(T')/H_p$. This is in accord with the ratio $\alpha_{\Lambda,T}/\alpha_{\Lambda,v} < 1$ found in the mixing-length analysis above. Concerning the absolute calibration, however, *the correlation length scales are smaller than the mixing-length values by as much as a factor of 5*. In an analogous comparison by Robinson et al. (2004) for subgiant atmosphere models, the vertical correlation lengths were also found to be smaller than the mixing

length used to construct the initial model, and the ratio varied significantly throughout the convection zone.

The horizontal correlation lengths L_H are shown in Figure 20, together with the vertical scales for comparison. For the velocity, the horizontal scale is much smaller than the vertical, indicative of eddies that are significantly elongated in the vertical direction. The temperature fluctuations appear to be much more symmetric, with only a small degree of elongation in the vertical direction, which is slightly more pronounced near the top of the convection
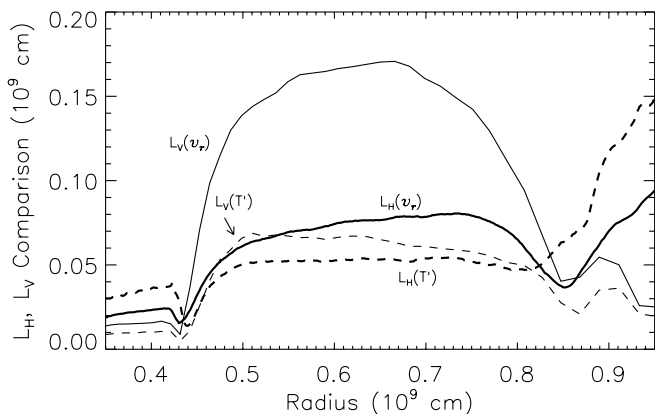

Fig. 20.—Horizontal and vertical correlation length scales, L_H (*thick line*) and L_V (*thin line*), shown for temperature (*dashed line*) and velocity (*solid line*) fluctuations.
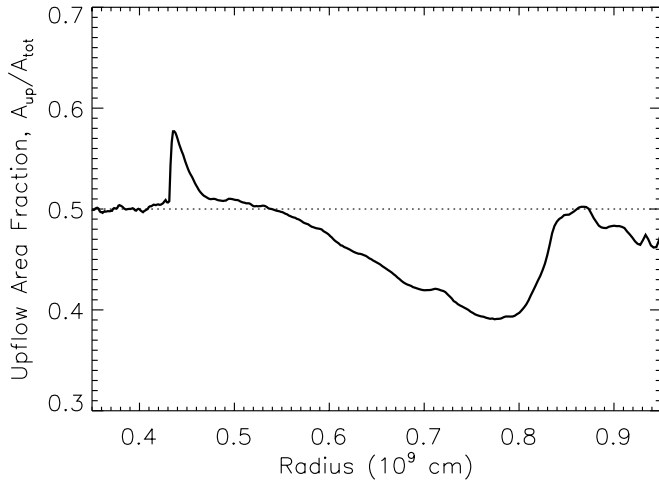
FIG. 21.—Fractional area occupied by the upward-flowing material f_u shown as a function of radial position. The downward-flowing area is $f_d = (1 - f_u)$, and the dashed line at $\frac{1}{2}$ indicates up-down symmetry.

zone. In the stable layers, the horizontal scales are larger than the vertical, which is a characteristic of the horizontal "sloshing" motions associated with g-modes.

6.4. The Kinetic Energy Flux, Flow Asymmetry, and Moving beyond the Mixing-Length Theory

The kinetic energy flux associated with convection is ignored in the MLT since it arises from the *asymmetries* in the flow and MLT assumes that the flow is symmetric. An order-of-magnitude estimate for the kinetic energy flux, however, can be made:

$$\frac{F_K}{F_c} \sim \frac{\rho v_c^2/2}{\rho c_p T'}\frac{v_c}{v_c} \sim \frac{\alpha_\Lambda}{8}\frac{\beta_T P}{T\rho c_p} = \frac{\alpha_\Lambda}{8}\nabla_{ad} \sim 0.04, \quad (25)$$

where mixing-length relationships have been used to calculate v_c and T', α_Λ is assumed to be of order unity, and $\nabla_{ad} \sim 0.25$ has been adopted from the simulation. This result tells us that

the kinetic energy flux will be a few percent of the convective enthalpy flux. This estimate is an upper limit since upflows and downflows will cancel to some degree (Böhm-Vitense 1992, their § 6.1). In the simulation, the ratio of kinetic to enthalpy flux is found to be $F_{K,\max}/F_{c,\max} \sim 0.01$, which is of order the simple MLT scaling, but down by a factor of a few as expected.

We can directly relate the kinetic energy flux to the flow asymmetry in the following way. The upflow area covering fraction $f_u = A_{up}/A_{tot}$ is shown in Figure 21. We can then write an estimate for the kinetic energy flux as

$$F_{K,net} = \tfrac{1}{2}\rho_0\left(f_u v_u^3 - f_d v_d^3\right), \quad (26)$$

which can be rewritten in terms of the flow velocities alone,

$$F_{K,net} = \frac{1}{2}\rho_0\left(\frac{v_u^3 + v_d^3}{v_u/v_d + 1} - v_d^3\right), \quad (27)$$

where we have used the mass conservation equation, $f_u v_u + f_d v_d = 0$, assuming $\rho_u \approx \rho_d$, which is a good approximation in these simulations. The kinetic energy flux in the simulation is shown in Figure 22, together with the value calculated according to equation (27), which shows good agreement. Here we have used the horizontal and time-averaged values for $\langle v\rangle$ and $\langle v^3\rangle$. The MLT, however, does not provide information about $\langle v^3\rangle$, but only $\langle v\rangle$. In order to find agreement with the simulation when using $\langle v\rangle^3$ in place of $\langle v^3\rangle$, a scaling factor is needed to account for the skewness in the radial velocity field. More precisely, the correlation coefficient $\chi = \overline{\langle v_u^3\rangle}/\langle v_u\rangle^3$ is needed, which is related to the skewness $\gamma = \langle v^3\rangle/\sigma_v^3$. Both χ and γ are presented in Figure 22. Note that the skewness is a good proxy for the downflow covering fraction ($f_d = 1 - f_u$; see Fig. 21), and therefore its sign is indicative of the direction of the kinetic energy flux.

Convective regions that are spanned by several pressure scale heights are found to have kinetic energy–to–enthalpy flux ratios larger than the few percent found in this study. For instance, the simulations of Cattaneo et al. (1991) and Chan & Sofia (1989), which each span ∼5 pressure scale heights, achieve
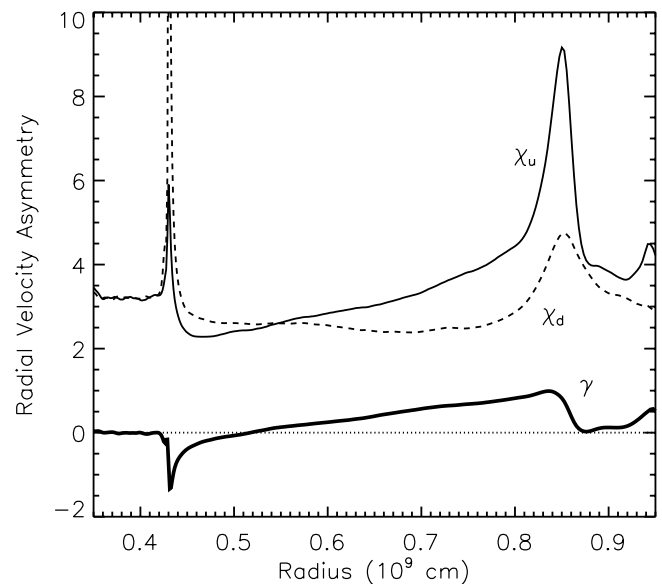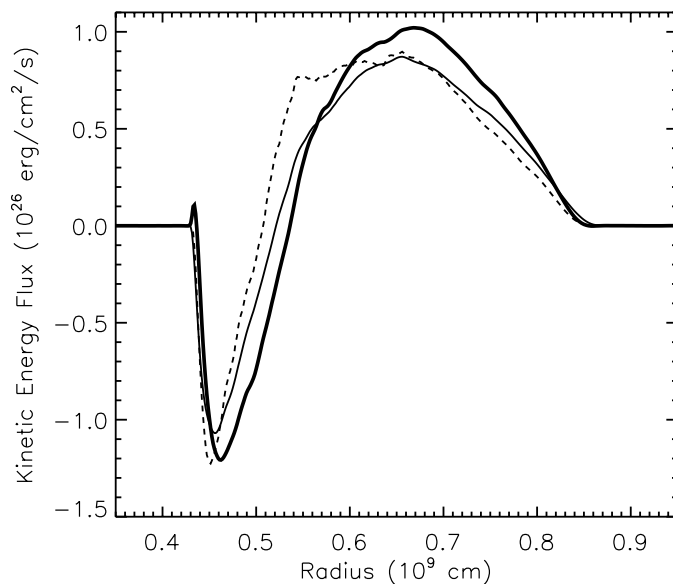
FIG. 22.—*Left*: Kinetic energy flux. The thick line shows the value measured in the simulation averaged over two convective turnovers; the thin solid line shows F_K calculated according to eq. (27); the thin dashed line shows F_K calculated according to eq. (27) but uses $c\langle v\rangle^3$ in place of $\langle v^3\rangle$ and a correlation constant of $c = 5$. *Right*: Asymmetries in radial velocity. The thick line shows the skewness in the velocity field, $\gamma = \langle v^3\rangle/\sigma_v^3$; the thin solid line and thin dashed line show the correlations $\chi_{u,d} = \langle v^3\rangle/\langle v\rangle^3$, where the subscripts u and d indicate upflows and downflows, respectively.

TABLE 4
Assumed and Measured Convection Parameters

Study	Pe[a]	α_E	$\alpha_{\Lambda,T}$	$\alpha_{\Lambda,v}$	α_Λ	L/H_p [b]	Grid Zoning
MLT	$\gg 1$	1	α	α	α	...	...
This study[c]	$\gtrsim 10^3$	0.70 ± 0.03	0.8–1.46	1.35–1.73	0.87–1.33	~2 (3.7)[d]	$100^2 \times 223$ (400)[b]
Chan-Sofia[e]	...	0.83 ± 0.03	1.32–3.75	3.39–6.4	1.90–4.4	4.8	$20^2 \times$ (≲50)
Kim[f]	...	0.80 ± 0.01	2.96–4.2	1.5–3.4	1.4–3.2	6	32^3
Robinson[g]	...	0.65–0.85	...	...	...	8.5	$114^2 \times 170$
Porter-Woodward[h]	$(10–8) \times 10^4$	0.7–0.9	4.08	3.82	2.68 (3.53)	4.5	$512^2 \times 256$

Note.—See § 6.2 for parameter definitions: $\alpha_{\Lambda,T} = 2\alpha_T$ and $\alpha_{\Lambda,v} = \sqrt{2}\alpha_v$, where α_T and α_v are defined by eqs. (23) and (24) and $\alpha_\Lambda = (\alpha_E \alpha_{\Lambda,v} \alpha_{\Lambda,T})^{1/2}$.

[a] The Péclet number is shown when provided by the author. In all cases the regions in the simulations for which parameter values are quoted were efficient convection, with $\Delta\nabla \lesssim 10^{-2}$, and excluded the superadiabatic layers in the surface convection models where parameters deviate significantly from those quoted here.

[b] The number of pressure scale heights spanned by the convectively unstable region.

[c] Model ob.3d.B; additional details in Table 2.

[d] The value in parentheses is for the region spanning the entire computational domain, including the stable bounding layers, with the other value referring to the convective region.

[e] In Chan & Sofia (1989) the range in α_T and $\alpha_{\Lambda,v}$ is calculated according to their Table 1 for the nearly adiabatic portion of the simulation where $10^{-3} < \Delta\nabla < 10^{-2}$.

[f] In Kim et al. (1996) the coefficient α_T is based on their Fig. 6. The coefficients $\alpha_{\Lambda,v}$ and α_Λ are plotted in their Fig. 9, and the range quoted in the table is for values at least 1 pressure scale height from the boundaries.

[g] In Robinson et al. (2004) only the correlation between radial velocity and temperature fluctuation is provided, which is a good surrogate for α_E. For the solar and subgiant cases see their Figs. 7–9.

[h] In Porter & Woodward (2000) the values for α_v, α_T, and α_Λ are quoted using the same definitions as in this study. The lower value quoted by these authors for α_Λ is a result of subtracting the kinetic energy flux from the enthalpy flux. The value in the parentheses is the mixing length α_Λ according to the definition in the table note above.

$|F_K/F_c| \sim 35\%$, and the domain in Chan & Sofia (1996) spanning ~ 7 pressure scale heights achieves $|F_K/F_c| \sim 50\%$. A key result in the analysis of Cattaneo et al. (1991) is that the kinetic energy flux is dominated by coherent, downward-directed flows that are correlated over distances comparable to the simulation domain. In addition, the enthalpy flux and kinetic energy fluxes associated with these downflows essentially cancel with $c_p T' \sim v_c^2$, which was shown to follow if the downflows can be described as Bernoulli streamlines.

Long range correlations, as well as the boundary effects that dominate our shell-burning model, undermine the accuracy of the basic MLT of convection. The large coherence of the flows seen in simulations, and present even in turbulent parameter regimes, suggests that modeling these *coherent structures* is a viable approach to improving the treatment of stellar convection. Already, models incorporating multiple streams or "plumes" to construct closure relations (e.g., Rempel 2004; Lesaffre et al. 2005; Belkacem et al. 2006; Kupka & Robinson 2007) are beginning to provide enticing alternatives to the MLT.

6.5. *Related Studies*

Although the mixing-length parameters calculated above deviate from constancy near the convective boundaries, a mean value is a good approximation throughout most of the convection zone. It would be interesting if these parameters α_E, α_T, and α_v were universal, as assumed by stellar modelers. If we restrict consideration to 3D compressible convection simulations for simplicity and homogeneity, there are several previous studies that have confronted MLT to which we can compare our results. These studies investigate convection under diverse conditions, including slab convection (Chan & Sofia 1987, 1989, 1996; Porter & Woodward 2000), a red giant envelope (Porter et al. 2000), and solar and subgiant surface layers (Kim et al. 1995, 1996; Robinson et al. 2003, 2004, 2005).

The number of zones used ranges from 1.9×10^4 (Chan & Sofia 1989) to 6.7×10^7 (Porter & Woodward 2000). The equations of state used include a gamma law (Chan & Sofia 1989; Porter & Woodward 2000), ionized gas (Kim et al. 1996; Robinson et al. 2004), and a combined relativistic electron plus ion gas (Timmes & Swesty 2000) in this paper. Subgrid-scale physics was

treated by a Smagorinsky model (Smagorinsky 1963) or by ignoring it. We note that Styne et al. (2000) have shown that PPM methods solving the Euler equations converge to the same limit as solutions to the Navier-Stokes equations, as resolution is increased and viscosity reduced. In addition, the subgrid-scale turbulence "model" implicit in the numerical algorithm of PPM is known to be well behaved (F. Grinstein 2006, private communication). Given this already inhomogeneous set of simulations, determining consistent convection parameters is difficult. Our attempt is given in Table 4, in which we summarize the convection parameters found in these studies for comparison to our own.

How well do these compare? In some respects the agreement is striking. The parameter α_E is in the range ~ 0.7–0.8 for all groups. Further, all agree that for their case, the MLT gives a fairly reasonable representation of the simulations in the sense that the alphas are roughly constant throughout the body of the convection zone. The difficulty is that the specific values of these alphas depend on the case considered. The two best-resolved simulations, ours and Porter & Woodward (2000), use the same solution method, PPM, yet have the most differing alphas. This suggests to us that the differences are due to the physical parameters of the respective convection zones. Porter et al. (2000) have already shown that slab geometry and spherical geometry give qualitatively different behavior for the alphas. Our shell is only 2 pressure scale heights in depth and is relatively slablike; Porter & Woodward (2000) have a convection zone that is more than twice as deep by this measure. There is a suggestion in Table 4 that the alphas increase with the depth of the convection zone. This would be reasonable if a convective plume were accelerated through the whole convection region before it is decelerated at the nonconvective boundary. However, the other differences mentioned above probably contribute to the scatter in the alpha parameters in Table 4.

Further efforts on this issue are needed. If convection does depend on the nonlocal, physical structure of the star, calibration of the mixing length to fit the Sun, as is traditionally done, is not wise. Furthermore, it is well known that the MLT is particularly prone to problems in the surface layers where convection becomes inefficient. Therefore, the empirical agreement of mixing-length
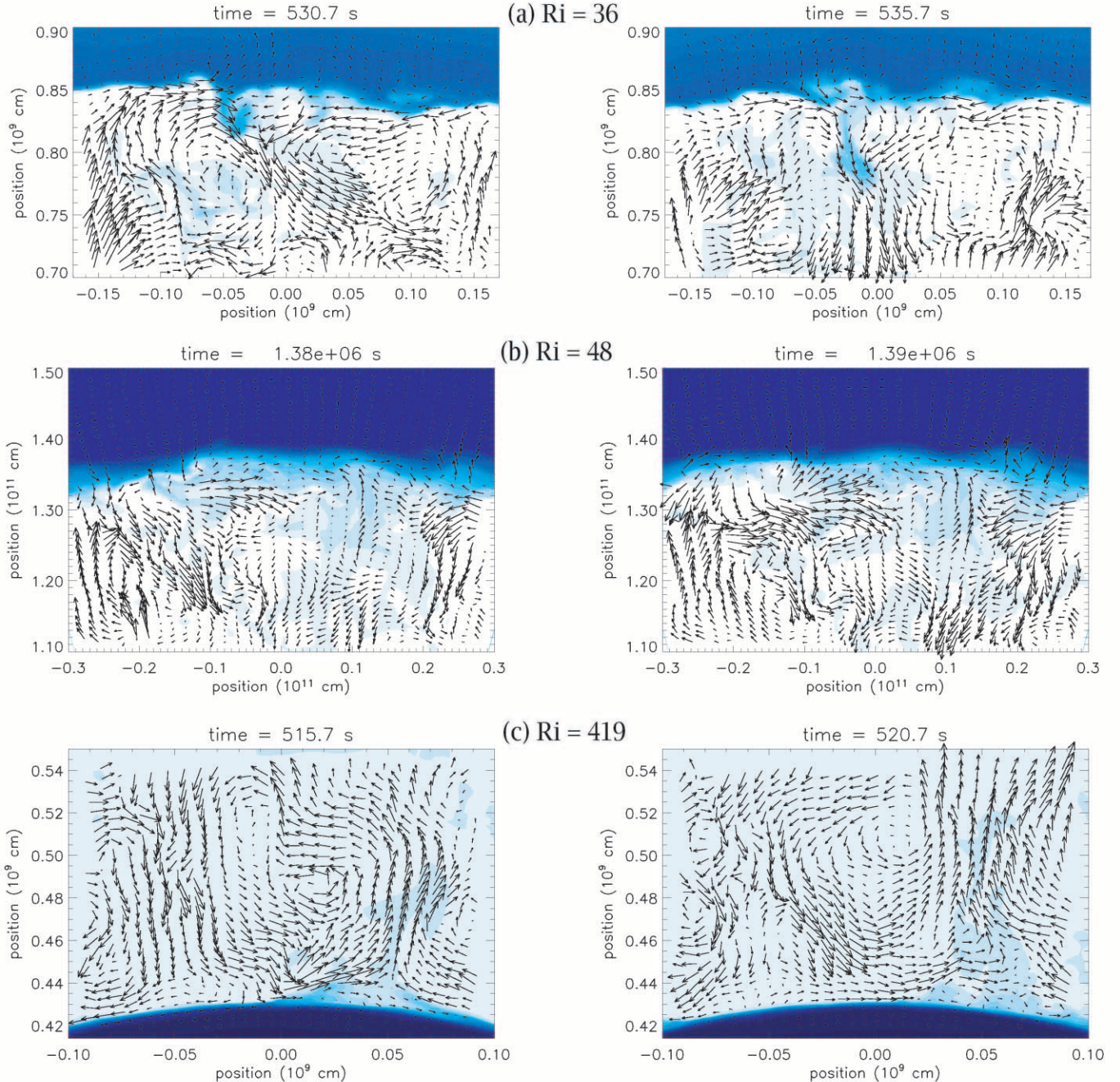
Fig. 23.—Equatorial slices showing the flow in the vicinity of the convective boundaries in the 3D simulations, ordered by relative stability: (*a*) upper shell convection boundary, $Ri_B \sim 36$; (*b*) core convection boundary, $Ri_B \sim 48$; (*c*) lower shell convection boundary, $Ri_B \sim 419$. The color map indicates composition abundance, where the darker tones trace stable layer material entrained across the interface. The velocity vectors have been sampled every third zone in each dimension.

calibration to the Sun and to Population II giants (Ferraro, et al. 2006) may be a fortuitous coincidence.

7. MIXING AT CONVECTIVE BOUNDARIES

The boundaries that separate the convective from the stably stratified layers in our 3D simulations span a range of relative stability, with $1 \lesssim Ri_B \lesssim 420$. At the lowest values of Ri_B, the boundary is quickly overwhelmed by turbulence, as described in § 4.1. Once Ri_B becomes large enough, the boundary stabilizes and evolves on a much longer timescale. Snapshots of the quasi-steady shell burning and the core convection boundaries are presented in Figure 23, ordered by Ri_B, which spans in the range $36 \lesssim Ri_B \lesssim 420$. The convective interface is composed of several components, including the turbulent convection zone, the distorted boundary layer of thickness h, and the stably stratified layer with internal wave motions (compare to Fig. 1).

As Ri_B increases, the boundary becomes more resilient to thickening and distortion by the turbulence. A region of partial mixing exists primarily on the turbulent side of the interface, where material is being drawn into the convection zone. The "ballistic" picture of penetrative overshooting (Zahn 1991), in which convective eddies are envisioned to pierce the stable layer, does not obtain. Instead, material mixing proceeds through instabilities at the interface, including shear instabilities and "wave breaking"
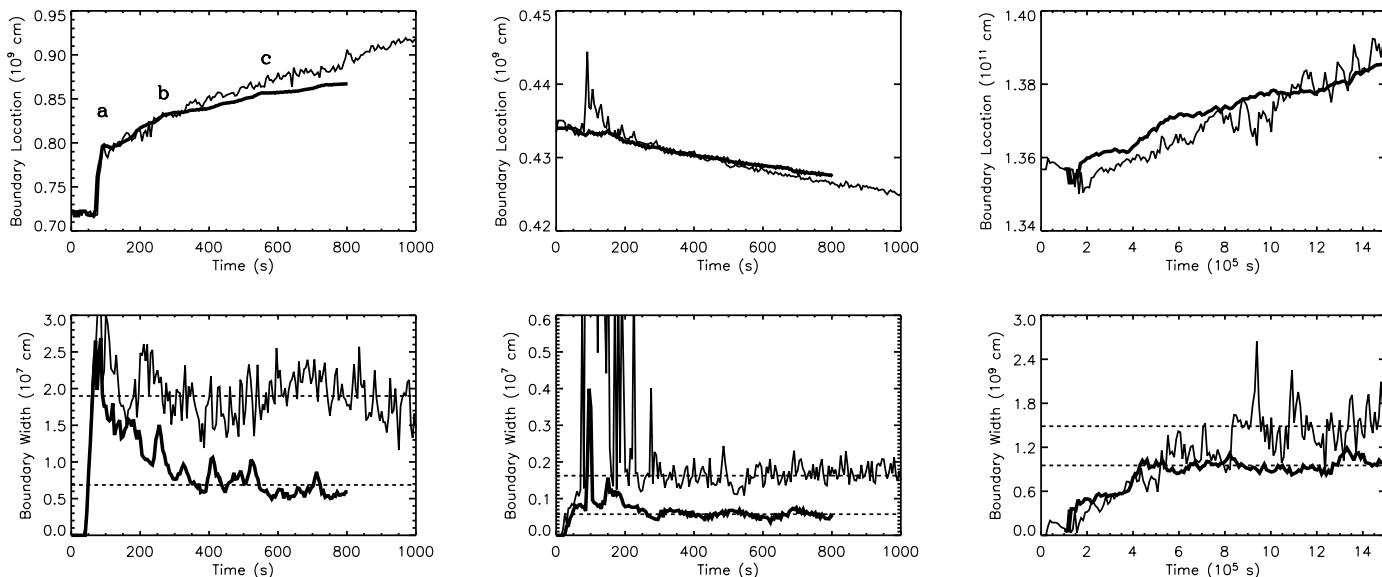
Fig. 24.—Time history of the convective boundary location (*top panels*) and the thickness of the convective interface (*bottom panels*) for upper shell burning boundary (*left panels*), lower shell burning boundary (*middle panels*), and core convection boundary (*right panels*). The thick line identifies the 3D models, ob.3d.B and msc.3d.B, and the thin line identifies the 2D models, ob.2d.e and msc.2d.b. The dashed lines show the averaged interface thickness for $t > 300$ s for oxygen burning and $t > 6.0 \times 10^5$ s for core convection. The letters a, b, and c in the top left panel mark times when the outward migration rate of the convective boundary rapidly adjusts to a new value in the 3D model.

events (Alexakis et al. 2004; Biello 2001), which break the boundary up into wisps of material that are then drawn into the turbulent region and mixed. The convective interface remains fairly sharp in all cases, and the effective width is well described by the elastic response of the boundary layer to incoming eddies, $h \sim v_c/N$. The convective interfaces seen in our simulations bear a striking resemblance to those observed in laboratory studies of turbulent entrainment of comparable Ri_B (see, e.g., McGrath et al. 1997, their Figs. 2–5).

The mixing that occurs due to the instabilities and eddy scouring events at the interface leads to a steady increase in the size of the convection zone. In this section we quantify the entrainment rates at the convective boundaries, we discuss these results in terms of the buoyancy evolution of the interface, and we describe how the "turbulent entrainment" process can be incorporated into a stellar evolution code as a dynamic boundary condition to be used in addition to the traditional static Ledoux and Schwarzschild criteria.

7.1. *Quantifying the Boundary Layer Mixing Rates*

As evident in Figure 23, the convective boundary layers are significantly distorted from spherical shells. To estimate the radial location of the interface, we first map out its shape in angle $r_i = r_i(\theta, \phi)$. At each angular position the surface is taken to be coincident with the radial position where the composition gradient is the steepest [this is comparable to the location of minimum density scale height $H_\rho = (\partial \ln \rho/\partial r)^{-1}$]. The interface thickness h is taken to be the rms variation of the surface r_i with angle, $h = \sigma[r_i(\theta, \phi)]$, which provides a quantitative measure of the amplitudes of the distortions imparted to the interface. The mass interior to the interface is calculated according to

$$M_i = \int_{r_0}^{\langle r_i \rangle} 4\pi r^2 \langle \rho \rangle \, dr, \qquad (28)$$

where r_0 is the inner boundary of the computational domain, $\langle \rho \rangle$ is the horizontally averaged density, and the mean interface ra-

dius is used for the upper limit on the integral. The time derivative $\dot{M}_i$ is the rate at which mass is entrained into the convection zone.

In Figure 24 the time histories of the averaged interface location $\langle r_i \rangle$ and interfacial thickness h are shown for the convective boundaries in our simulations. A 3D model and a representative 2D model are shown for each boundary. The outer shell boundary layer adjusts rapidly in the first 100 s to a new position, due to the penetration event discussed in § 4.1, after which a slow outward migration ensues. For the 3D shell convection model, the outward migration proceeds in distinct stages, labeled "a," "b," and "c" in Figure 24. Each stage is well described by a linear increase of radius with time and ends with a rapid adjustment to a new entrainment rate. This behavior can also be seen in Figure 4, where the change in entrainment rate coincides with changes in the background composition gradient and stability (compare to the initial buoyancy frequency profile in Fig. 2).

The downward migration of the lower shell boundary is more uniform and proceeds at a significantly reduced rate compared to the upper boundary. The core convection boundary evolution departs most significantly from a linear trend, but monotonic growth is clearly established very soon after the simulation begins, $t \gtrsim 2 \times 10^5$ s.

The interfacial thickness h in the oxygen-burning models is initially large due to the strong mixing event during the initial transient but settles down to a relatively constant value for $t \gtrsim 300$ s. In contrast, the boundary thickness in the core convection model increases gradually with time until a steady state value is achieved, due to the milder initial development. In all cases, the time-averaged values of h during the quasi–steady states compare well to the boundary displacement expected for eddies impacting the stable layer with the characteristic convective velocities, $h \sim v_c/N$.

The entrainment rate and the interfacial thickness are larger in all of the 2D models as a consequence of the larger velocity scales. The interface migration rates and averaged interfacial layer thicknesses are tabulated for all of the models in Tables 5 and 6 and are broken down into various time intervals over which linear growth

TABLE 5
Convective Boundary Layer Properties for Oxygen Shell Burning Models

Model	Time Interval $(10^2$ s)	$\bar{r}_i$ $(10^9$ cm)	$\bar{h}$ $(10^7$ cm)	$\dot{\bar{r}}_i$ $(10^4$ cm s$^{-1})$	$\overline{v_{exp}}$ $(10^4$ cm s$^{-1})$	$\sigma[v_H]$[a] $(10^7$ cm s$^{-1})$	$\overline{\Delta b}$[b] $(10^7$ cm s$^{-2})$	$\log \overline{E}$	$\overline{Ri_B}$
ob.3d.B	[1.5, 2.7]	0.816	1.287	25.766 ± 0.869	0.6	0.313	0.574	-1.095	21.8
	[2.7, 5.5]	0.842	0.797	8.252 ± 0.180	0.6	0.316	0.966	-1.616	36.0
	[5.5, 8.0]	0.861	0.586	5.171 ± 0.179	0.6	0.281	1.062	-1.789	50.0
ob.2d.c	[3.5, 5.7]	0.857	0.191	10.620 ± 0.816	0.9	1.385	1.422	-2.154	5.9
ob.2d.C	[2.0, 4.0]	0.830	1.776	19.117 ± 0.988	0.5	1.436	1.010	-1.887	3.2
ob.2d.e	[3.5, 8.0]	0.868	1.900	10.021 ± 0.319	2.5	1.464	1.334	-2.289	4.4
ob.3d.B	[3.0, 8.0]	0.429	0.057	-0.700 ± 0.009	0.50	0.479	30.686	-2.601	418.6
ob.2d.c	[3.5, 5.7]	0.428	0.201	-1.686 ± 0.058	1.05	1.769	33.739	-2.811	86.3
ob.2d.C	[2.0, 4.0]	0.430	0.193	-1.625 ± 0.072	0.65	1.434	32.160	-2.780	101.7
ob.2d.e	[3.5, 8.0]	0.429	0.162	-0.975 ± 0.018	1.20	1.645	32.620	-2.879	84.4

[a] The rms fluctuations in the horizontal velocity at the interface location.
[b] The buoyancy jump across the interface.

of the boundary is a good approximation. Time-averaged mass entrainment rates are also included in Tables 2 and 3.

7.2. The Entrainment Energetics

In order for entrainment to take place at a convective boundary, the buoyancy increment of the stable layer material over that of the mixed layer material must be overcome. This can happen in two distinct ways. First, nonadiabatic processes can change the relative stability of the stable layer. For example, heating the convective region will cause an increase in its entropy, and the buoyancy jump separating the overlying layer will decrease. The rate at which the convective boundary will grow due to heating is $u_s = \dot{s}/(\partial_r s)$, where $\partial_r s$ is the radial gradient of entropy at the boundary and $\dot{s}$ is the time rate of change of entropy in the shell. This process will cause both the upper and lower boundaries to migrate to larger radii: the upper boundary will be weakened, while the lower boundary will become stiffer. Nonadiabatic processes in the boundary layers will affect their stability in the same way: cooling in the upper and heating in the lower boundaries will weaken their stratification.

A related but distinct process is turbulent entrainment, whereby turbulent kinetic energy does work against gravity to draw material into the turbulent region. In this process, the stratification is weakened at a convective boundary by the turbulent velocity fluctuations. This is quantified in terms of the buoyancy flux $q = g\rho'v'/\rho_0$. In the absence of heating and cooling sources the buoyancy in the interfacial layers will evolve according to the buoyancy conservation equation,

$$\partial_t b = -\text{div}(q), \qquad (29)$$

and a positive flux divergence at the boundary will lead to a weakening of the stratification. The relationship between turbulent entrainment and the weakening of a boundary through heating and cooling can be understood in terms of the enthalpy flux that attends the buoyancy flux. In fact, the buoyancy flux is directly related to the enthalpy flux across the interface,

$$F_c = \rho_0 c_P \langle T' v_r' \rangle = \frac{c_P T_0}{\beta_T} \langle \rho' v_r' \rangle = \rho_0 c_P \frac{T_0}{\beta_T g} q, \qquad (30)$$

and is equivalent to heating and cooling processes operating in the boundary layer (note the downward-directed enthalpy flux within the boundary layers in Fig. 15).

What drives the entrainment seen in the present simulations? Can the entrainment in the outer shell boundary be explained by the heating of the convection zone by nuclear burning? Comparing the entropy growth rate of the shell to the entropy gradient at the boundary, we find $u_s \sim 0.8 \times 10^4$ cm s^{-1}, which is at most 17% of the measured growth rate for this boundary, and typically of order a few percent. Shell heating will reduce the growth rate of the lower boundary by $u_s \sim 0.04 \times 10^4$ cm s^{-1}, which is of order a few percent of the rate measured. Therefore, the overall heating and cooling of the shell contribute very modestly to the growth of the shell over the course of the simulation. The long thermal timescale in the core convection model reduces this effect even more, where it is lower by several orders of magnitude. Therefore, we turn to the turbulent hydrodynamic processes operating in the boundary layer to understand the growth of the convection zones.

In Figure 25 we present the buoyancy flux profiles for our 3D simulation models, including both time series diagrams and time-averaged radial profiles. The properties of the buoyancy flux can be divided into three distinct flow regimes: (1) the body of the buoyant convecting layer, which is dominated by positive q; (2) the convective boundary layers, with negative q; and (3) the stably stratified layers, where q is oscillatory but has a nearly zero mean (in both a horizontal and time-average sense).

TABLE 6
Convective Boundary Layer Properties for "Core Convection" Models

Model	Time Interval $(10^5$ s)	$\bar{r}_i$ $(10^{11}$ cm)	$\bar{h}$ $(10^9$ cm)	$\dot{\bar{r}}_i$ $(10^3$ cm s$^{-1})$	$\overline{v_{exp}}$[a] $(10^2$ cm s$^{-1})$	$\sigma[v_H]$ $(10^5$ cm s$^{-1})$	$\overline{\Delta b}$ $(10^2$ cm s$^{-2})$	$\log \overline{E}$	$\overline{Ri_B}$
msc.3d.B	[6.0, 10.0]	1.374	0.949	1.754 ± 0.080	...	2.011	6.07	-2.0594	66
	[10.0, 12.0]	1.378	0.897	-0.020 ± 0.140	...	1.878	5.83	...	72
	[12.0, 15.0]	1.382	0.998	2.731 ± 0.099	...	2.411	5.70	-1.9459	48
msc.2d.b	[6.0, 10.0]	1.369	1.319	1.401 ± 0.390	...	8.070	6.43	-2.7604	9.2

[a] The expansion velocity in these models remains very small with $v_{exp} < 10$ cm s^{-1}.
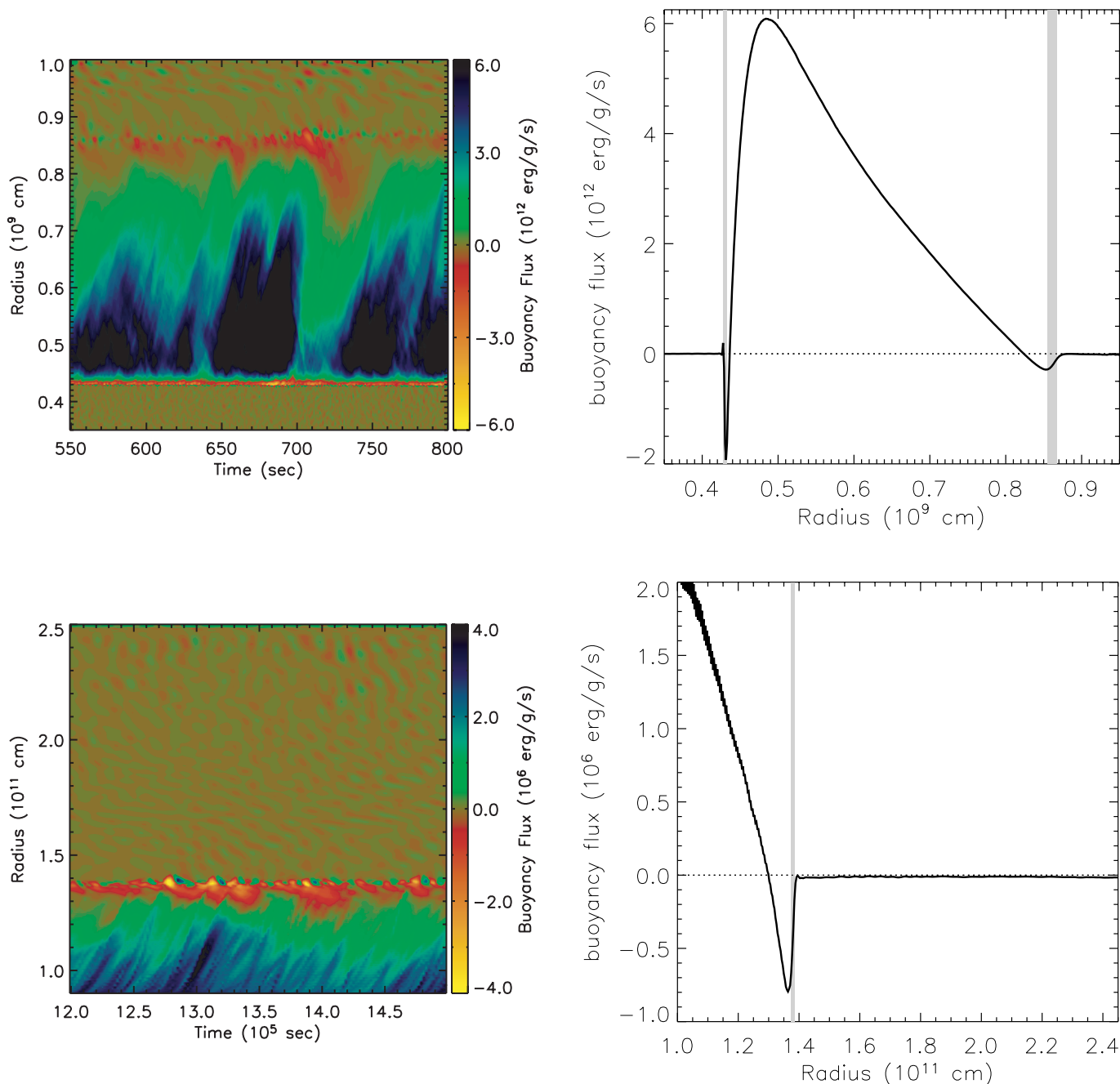
FIG. 25.—Buoyancy flux. Time series diagrams and time-averaged radial profiles are shown for the 3D oxygen shell burning model (*top panels*) and the 3D core convection model (*bottom panels*).

The buoyancy driving of the convective flow in regime 1 can be appreciated by comparing the flow velocity to the commonly used buoyant convection velocity scale $v_*^3 = 2.5 \int \langle q \rangle \, dr$, where integration is taken over the radial extent of the convection zone (see, e.g., Deardorff 1980). In the 3D shell-burning and core convection models $v_* \sim 10^7$ and $\sim 3 \times 10^5$ cm s^{-1}, respectively, which compares well with the turbulent radial velocity fluctuations measured in the simulation (Figs. 6 and 12).

In regime 2, which occurs in the convective boundaries, the buoyancy flux is negative. A negative value of q indicates that turbulent kinetic energy is being converted into potential energy. The mixing associated with this negative buoyancy flux underlies the entrainment that is taking place at the boundaries through equation (29). We demonstrate this by showing that the entrain-

ment speeds measured in the simulation are consistent with the measured buoyancy fluxes. The interface migration speed is incorporated into the conservation equation by writing the time derivative as an advective derivative,

$$\partial_t b \sim u_e \partial_r b = u_e N^2, \tag{31}$$

where we have used the relationship $\partial_r b = N^2$. Using this time derivative in equation (29) and solving for u_e, we find

$$\tilde{u}_e = \frac{\Delta q}{h N^2}, \tag{32}$$

where we have approximated the divergence of the buoyancy flux with the difference $\Delta q/h$. We use the symbol $\tilde{u}_e$ to

distinguish the calculated rate from the values measured in the simulation.

If we adopt the buoyancy flux at the interface for Δq (Fig. 25), the measured interface thickness h, and the buoyancy frequency at the boundary, we find the following entrainment rates. For the upper shell boundary, lower shell boundary, and the core convection boundary we have $\tilde{u}_e \sim 5.1 \times 10^4$, 1.1×10^4, and 2.2×10^3 cm s^{-1}, respectively. These are to be compared with $u_e = |\dot{r}_i - v_{\text{exp}}|$ measured in § 7.1 and presented in Tables 5 and 6. The values corresponding to the same time period are $u_e = 4.6 \times 10^4$, 1.2×10^4, and 2×10^3 cm s^{-1}. Although these calculated rates are only order of magnitude estimates (e.g., we use the crude approximation for the time derivative in eq. [31]), they compare well to the values measured in the simulations, and the buoyancy flux due to turbulent entrainment can account for the growth of the convective layers seen here.

7.3. *Whence q?*

The buoyancy flux q appears as a term in the turbulent kinetic energy (TKE) equation, which we present in Appendix A (eq. [A13]). In our notation, the buoyancy flux is related to the buoyancy work term by $q = \langle W_B \rangle / \rho_0$. The buoyancy flux, therefore, is related to the rate at which turbulent kinetic energy is advected into the stable layer F_K, the rate at which it dissipates through viscous forces ε_K, and the rate at which energy is transported through the boundary layer by pressure-velocity correlations F_p. In essence, entrainment is the process by which the turbulent kinetic energy in the boundary layer does work against gravity to increase the potential energy of the overall stratification.

Two theoretical approaches have been taken to study entrainment. The first approach ignores the TKE equation and instead posits an "entrainment law." The entrainment law is merely a functional form for the rate at which stable layer mass will flow into the turbulent region and is therefore a dynamic boundary condition. These laws are usually parameterized by the stability properties of the interface and the strength of the turbulence through Ri_B (see, e.g., Fedorovich et al. 2004). Once an entrainment law is adopted, the enthalpy flux can be calculated and the evolution of the boundary can be self-consistently solved for. The advantage of such an entrainment law is the simplicity with which it can be incorporated into global circulation models of the atmosphere, for instance.

An alternative approach to adopting an entrainment law is an explicit physical model for the terms in the TKE equation (eq. [A13]). For example, general forms for the buoyancy flux profile within the stable layer have been applied with some success in reproducing the growth of the atmospheric boundary layer and the deepening of the oceanic thermocline (Stull 1976b; Deardorff 1979; Fedorovich & Mironov 1995). In some respects, however, these models are glorified entrainment laws since the buoyancy flux is prescribed in a simplified, parameterized way. Moving beyond assumptions concerning the turbulence profiles within the interfacial layer are theoretical models that take into account the interactions of waves and turbulence and incorporate nonlinear models for the evolution of instabilities (e.g., Carruthers & Hunt 1986; Fernando & Hunt 1997). The approach adopted in these theoretical studies is general enough that any adjustable parameters may turn out to be universal and a predictive model can be developed. In addition, the framework employed is general enough that the production of turbulence by mean flows (i.e., stellar rotation) can be incorporated, as well as long-range effects due to internal waves. The internal waves are incorporated through the pressure correlation flux, F_p, and play a
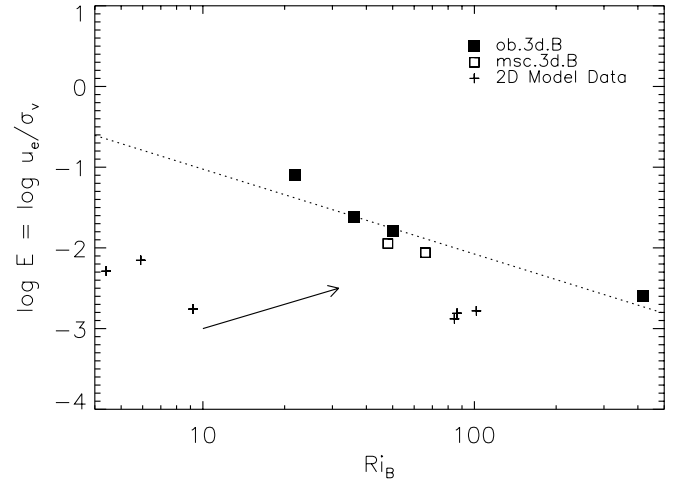

FIG. 26.—Normalized entrainment rate plotted against bulk Richardson number Ri_B. The 3D models are marked with squares, and the 2D data with plus signs. The best-fit power law to the 3D model data is shown by the dashed line. The 2D entrainment rates fall everywhere below the 3D trend. The arrow indicates the direction in the diagram that the 2D data points would move if the effective rms turbulence velocity were lower.

central role in the evolution of the buoyancy flux when wave breaking is important.

7.4. *An "Empirical" Entrainment Law*

The development of a sophisticated turbulence model to explain entrainment is beyond the scope of the present work. Instead, we ask, to what extent do the entrainment laws used in geophysical models apply to our simulations and stellar interiors? Guided by laboratory study and geophysical large eddy simulation, we study the dependence of the entrainment rate on the bulk Richardson number.

We calculate Ri_B according to equation (2), using the horizontal correlation length scale $L = \mathcal{L}_H$ defined in Appendix B. The buoyancy jump is calculated by performing the integration in equation (3) over the interface in the interval $r \in [\overline{r_i} - h, \overline{r_i} + h]$. The normalized entrainment rates $E = u_e / \sigma$, the buoyancy jumps Δb, and Ri_B are listed in Tables 5 and 6. The dependence of the entrainment coefficient E on Ri_B is presented in Figure 26.

The 2D and 3D data are found to obey similar trends (lower E for higher Ri_B) but occupy significantly different regions of the diagram. This can be explained by the much higher rms velocities in the 2D simulation. The velocity scale in 2D is apparently an artifact of the reduced dimensionality of the problem, which significantly influences the flow morphology. Although the velocity scale is higher in the 2D models, it is much more laminar and accompanied by less turbulent mixing. The arrow in Figure 26 indicates the direction that the 2D data points would move if a lower effective rms velocity were assumed. In what follows we focus our attention exclusively on the entrainment data found for the more realistic 3D models.

We find that the entrainment coefficient E is well described by a power-law dependence on Ri_B of the form in equation (5). Our best-fit values for the parameters are $\log A = 0.027 \pm 0.38$ and $n = 1.05 \pm 0.21$. This entrainment law is shown by a dashed line in Figure 26. Remarkably, the power law is of order unity, in agreement with geophysical and laboratory studies. The fact that the entrainment in our simulations is governed by the same, fairly universal dependence on Ri_B as these other studies may have been anticipated, considering the striking degree of similarity between the buoyancy profiles and the character of the developed flow in the vicinity of the boundary (Fig. 23).

7.5. *A Dynamic Convection Zone Boundary Condition*

Mass entrainment is a fundamentally different phenomenon from diffusion, the typical treatment used to incorporate new mixing mechanisms into a stellar evolution code. Therefore, how might we incorporate this new process? Schematically, the idea is very simple. For each convective boundary, initially found with the traditional stability criteria ($\partial s/\partial r = 0$, $\partial^2 s/\partial r^2 \neq 0$), we can calculate the associated bulk Richardson number based on the background stratification and an approximation of the turbulence characteristics (e.g., from MLT). With Ri_B in hand we can then input this into our entrainment law, $E = E(\text{Ri}_B)$, which returns to us the entrainment rate. The entrainment rate, therefore, is the boundary growth rate as a function of Ri_B and possibly other parameters of the system. The function $E(\text{Ri}_B)$ can be broken up into at least three regimes for convenience:

1. *Low stability:* $\text{Ri}_B < \text{Ri}_B^{\min}$.—For low Ri_B it is observed that mass entrainment happens very quickly, on an advection time-scale (§ 4.1). Therefore, we can define a minimum $\text{Ri}_B^{\min}$ at which the expansion of the convection zone will proceed rapidly, eliminating convective boundaries that are too weak to support the adjacent turbulence.

2. *Intermediate stability:* $\text{Ri}_B^{\min} < \text{Ri}_B < \text{Ri}_B^{\max}$.—For an intermediate range of stability, we can use the fairly universal entrainment law that matches our simulation data, defined by the two parameters A and n. Although the mixing rates are found to scatter around the best-fit law, the general monotonic, power-law dependence is found to be robust. We can incorporate this physics into the stellar evolution code as a mass entrainment rate,

$$\dot{M}_E = \frac{\partial M}{\partial r} u_E = \left(4\pi r_i^2 \rho_i\right)\sigma_H f_A \times 10^{(-n\log \text{Ri}_B)}, \quad (33)$$

where the normalization factor is written as $f_A = 10^{(\log A)}$ and represents the turbulent entrainment mixing efficiency. More sophistication can subsequently be incorporated as our understanding of the entrainment process improves.

3. *High stability:* $\text{Ri}_B > \text{Ri}_B^{\max}$.—The entrainment process will cease to operate at some upper limit $\text{Ri}_B^{\max}$, above which the boundary evolution will be controlled by diffusive processes on the molecular scale. Following Phillips (1966), we have

$$\text{Ri}_B^{\max} \simeq \left(\frac{u_E}{\sigma}\right)\left(\frac{\sigma L}{\kappa}\right), \quad (34)$$

which is based on the condition that the kinetic energy in the turbulence is sufficient to lift the material from the interface, $\rho\sigma^2 \gtrsim \rho N^2 \Delta^2$. Here the interface thickness is taken to be that due to molecular diffusion with $\Delta \gtrsim \kappa/u_E$. The relatively small diffusion rates in stellar interiors imply that turbulent entrainment will continue to operate to very high Richardson numbers. For comparison, the entrainment process in the ocean is estimated to operate up to $\text{Ri}_B \sim 10^5$–10^6.

Additional details concerning the implementation of this type of boundary condition into TYCHO will be presented in a subsequent paper.

8. SUMMARY AND CONCLUSIONS

In this paper we have presented the results of 3D, reactive, compressible, hydrodynamic simulations of deep, efficient stellar convection zones in massive stars. Our models are unique in terms of the degree to which nonidealized physics have been used and the evolutionary stages simulated, with fuel and ash clearly distinguished.

We find several general results regarding the basic properties of the convective flow:

1. The flow is highly intermittent but has robust statistical properties.

2. The 2D and 3D velocity scales differ by a factor of several, and the flow morphologies are completely different.

3. Stable layers interact with convection to decelerate plumes and consequently distort these layers, which then generate waves.

4. Mixing is found to occur at convective boundaries in a manner best described as turbulent entrainment, rather than the traditional picture of convective overshooting wherein turbulent eddies ballistically penetrate the stable layers.

We have compared our oxygen shell burning model to MLT assumptions. We show that, while a reasonable representation of the superadiabatic temperature gradient and velocity scale can be fitted with a single mixing length, the values of the inferred mixing-length "constants" differ from other simulations. This was already implied in Porter et al. (2000), who found differences for slab and spherical geometries. There may be a dependence on the depth of the convection zone as well, and possibly on the nature of the stable boundary regions and/or the nature of the driving process (burning or radiative loss).

Why do we care about MLT in regions of efficient convection? The reasons are as follows: (1) the temperature profile can affect the burning rates, which have a stiff temperature dependence; (2) the velocity scale can affect the nucleosynthesis (such as *s*-process branching ratios in double shell burning AGB stars) by dictating the exposure time of the plasma to varying conditions throughout the burning region; and (3) the velocity scale and the kinetic energy flux are an important input needed for calculating the mixing at convective boundaries.

We have found that the extent of mixing is better represented by an integrated Richardson number rather than the conventional Schwarzschild or Ledoux criteria alone. This incorporates physics related to the resistance of stiff boundaries to mixing. Related to the definition of boundary stiffness, we have identified an important physical process that is missing from the standard theory of stellar evolution: turbulent entrainment. This process is well known in the meteorology and oceanographic communities and has been extensively studied experimentally. We show that the rate of entrainment in our simulations is well represented by a simple function of the buoyancy jump in a manner similar to that measured in relevant experiments.

The long-term consequences of convective boundary inconsistencies such as the one illustrated by the initial transient in our simulation, and for which the conditions are common in 1D stellar models, can significantly alter the size of convective cores and thus the subsequent explosion and nucleosynthetic yields of the resultant supernova. In a subsequent paper in this series, we will present case studies that incorporate the physical insight gained through these simulations into the TYCHO stellar evolution code. We expect to see effects in solar models, *s*-processing in AGB stars, stellar core formation (white dwarfs, neutron stars, and black holes), stellar nucleosynthesis yields, stellar ages, and H-R diagrams.

APPENDIX A

THE ENERGY EQUATION

A1. TOTAL ENERGY

The primitive energy equation solved by PROMPI is

$$\partial_t(\rho E) + \nabla \cdot [(\rho E + p)\boldsymbol{u} + \boldsymbol{F}_r] = \rho \boldsymbol{u} \cdot \boldsymbol{g} + \rho \epsilon_{\text{net}}, \tag{A1}$$

where the total energy is composed of the internal and kinetic components, $E = E_I + E_K$. We decompose the velocity, density, and pressure fields into mean and fluctuating components according to

$$\varphi = \varphi_0 + \varphi', \tag{A2}$$

where $\overline{\langle \varphi \rangle} = \varphi_0$ and $\overline{\langle \varphi' \rangle} = 0$. The overbar and brackets indicate time and horizontal averaging, respectively. The pressure-velocity correlation term is

$$\nabla \cdot \overline{\langle p\boldsymbol{u} \rangle} = \nabla \cdot \overline{\langle p_0\boldsymbol{u}_0 \rangle} + \nabla \cdot \overline{\langle p_0\boldsymbol{u}' \rangle} + \nabla \cdot \overline{\langle p'\boldsymbol{u}_0 \rangle} + \nabla \cdot \overline{\langle p'\boldsymbol{u}' \rangle}. \tag{A3}$$

The gravity term is

$$\overline{\langle \rho \boldsymbol{g} \cdot \boldsymbol{u} \rangle} = \overline{\langle \rho_0\boldsymbol{u}_0\boldsymbol{g} \rangle} + \overline{\langle \rho_0\boldsymbol{u}'\boldsymbol{g} \rangle} + \overline{\langle \rho'\boldsymbol{u}_0\boldsymbol{g} \rangle} + \overline{\langle \rho'\boldsymbol{u}'\boldsymbol{g} \rangle}. \tag{A4}$$

The averaging operator eliminates terms that are first order in fluctuations (by definition), and we have

$$\partial_t\overline{\langle \rho E \rangle} + \nabla \cdot \left[\overline{\langle \rho E\boldsymbol{u}_0 \rangle} + \overline{\langle \rho E\boldsymbol{u}' \rangle} + \overline{\langle p_0\boldsymbol{u}_0 \rangle} + \overline{\langle p'\boldsymbol{u}' \rangle} + \boldsymbol{F}_r \right] = \overline{\langle \rho_0\boldsymbol{u}_0\boldsymbol{g} \rangle} + \overline{\langle \rho'\boldsymbol{u}'\boldsymbol{g} \rangle} + \overline{\langle \rho \epsilon_{\text{net}} \rangle}. \tag{A5}$$

We can further simplify this expression using the condition of hydrostatic equilibrium, which holds to a high degree of accuracy in the simulation ($\nabla p_0 = \rho_0 \boldsymbol{g}$). The background velocity in this case, $\boldsymbol{u}_0$, is a slow, highly subsonic expansion or contraction that is driven on a thermal timescale. The background velocity field has only a radial component (i.e., there is no rotation in the current model), $\boldsymbol{u}_0 = (u_{0,(r)}, 0, 0)$. The energy equation can be then simplified to read

$$\partial_t\overline{\langle \rho E \rangle} + \nabla \cdot \overline{\langle \rho E\boldsymbol{u}_0 \rangle} = -\nabla \cdot \overline{\langle \boldsymbol{F}_p + \boldsymbol{F}_I + \boldsymbol{F}_K + \boldsymbol{F}_r \rangle} - \overline{\langle p_0\nabla \cdot \boldsymbol{u}_0 \rangle} + \overline{\langle W_b \rangle} + \overline{\langle \rho \epsilon_{\text{net}} \rangle}, \tag{A6}$$

where we have used the following definitions:

$$\boldsymbol{F}_r = -k_r\nabla T, \tag{A7}$$

$$\boldsymbol{F}_I = \rho E_I\boldsymbol{u}', \tag{A8}$$

$$\boldsymbol{F}_K = \rho E_K\boldsymbol{u}', \tag{A9}$$

$$\boldsymbol{F}_p = p'\boldsymbol{u}', \tag{A10}$$

$$\boldsymbol{W}_b = \rho'\boldsymbol{g} \cdot \boldsymbol{u}', \tag{A11}$$

with radiative "conductivity" $k_r = 4acT^3/(3\kappa_R\rho)$ and Rosseland mean opacity κ_R.

A2. KINETIC ENERGY

The kinetic energy equation is derived by forming the scalar product of the velocity with the equation of motion (e.g., Shu 1992, pp. 14–24). The kinetic energy equation can be written in vector form as

$$\partial_t(\rho E_K) + \nabla \cdot (\rho E_K\boldsymbol{u}) = -\boldsymbol{u} \cdot \nabla p + \rho \boldsymbol{u} \cdot \boldsymbol{g}. \tag{A12}$$

Again, we decompose the fields into mean and fluctuating components, employ the hydrostatic equilibrium condition, and perform averages. The result is

$$\partial_t\overline{\langle \rho E_K \rangle} + \nabla \cdot \overline{\langle \rho E_K\boldsymbol{u}_0 \rangle} = -\nabla \cdot \overline{\langle \boldsymbol{F}_p + \boldsymbol{F}_K \rangle} + \overline{\langle p'\nabla \cdot \boldsymbol{u}' \rangle} + \overline{\langle W_b \rangle} - \varepsilon_K. \tag{A13}$$

Here ε_K is the viscous dissipation of kinetic energy. In our simulations, this term is not modeled explicitly and arises due to numerical dissipation. The term $p'\nabla \cdot \boldsymbol{u}'$ represents the compressional work done by turbulent fluctuations, and the other terms are as defined above.

APPENDIX B

CORRELATION LENGTH SCALES

The vertical correlation of the horizontal distribution of fluctuations in a quantity $X' = X - \langle X \rangle$ at radial position r and offset position $r + \delta r$ is calculated according to

$$C^V(\delta r;\, r) = \frac{1}{\Delta\Omega} \frac{\int X'(r,\, \theta,\, \phi) X'(r + \delta r,\, \theta,\, \phi)\, d\Omega}{\sigma_X(r)\sigma_X(r + \delta r)}, \tag{B1}$$

where the integral is taken over the angular direction with $d\Omega = \sin\theta\, d\theta\, d\phi$. The correlation is normalized by the product of the horizontal rms value of the quantity at the two levels being compared σ_X.

The horizontal correlation of fluctuations at radial position r is calculated using the autocorrelation function,

$$C^H(\delta s;\, r) = \frac{\langle X'(r,\, s) X'(r,\, s + \delta s)\rangle}{\sigma_X(r)^2}, \tag{B2}$$

where the angle brackets denote averaging over all horizontal locations s and fixed offset δs. The horizontal correlation is normalized by the variance of the quantity σ_X^2.

Characteristic length scales are defined as the offset position where the correlation function drops to a value of 0.5. For horizontal correlations, we define this length as $\mathcal{L}_H$. We also define a value that is twice this length, the FWHM, which we denote by L_H. [The value $\mathcal{L}_H$ provides a good approximation to the integral scale, $\int C^H(\delta s;\, r)\, d\delta s$.]

In the vertical direction the sign of the offset δr is retained and a separate length scale is defined where the correlation function drops to 0.5 for positive and negative offsets, which we denote by L_V^+ and L_V^-. The full width is denoted $L_V = L_V^+ - L_V^-$.

REFERENCES

Alexakis, A., et al. 2004, Phys. Fluids, 16, 3256
Alexander, D. R., & Ferguson, J. W. 1994, ApJ, 437, 879
Arnett, D. 1972, ApJ, 173, 393
———. 1996, Supernovae and Nucleosynthesis: An Investigation of the History of Matter, from the Big Bang to the Present (Princeton: Princeton Univ. Press)
Asplund, M., Grevesse, N., & Sauval, A. J. 2005, in ASP Conf. Ser. 336, Cosmic Abundances as Records of Stellar Evolution and Nucleosynthesis, ed. T. G. Barnes III & F. N. Bash (San Francisco: ASP), 25
Aufderheide, M. B. 1993, ApJ, 411, 813
Beaudet, G., Petrosian, V., & Salpeter, E. E. 1967, ApJ, 150, 979
Belkacem, K., Samadi, R., Goupil, M. J., & Kupka, F. 2006, A&A, 460, 173
Biello, J. A. 2001, Ph.D. thesis, Univ. Chicago
Böhm-Vitense, E. 1958, Z. Astrophys., 46, 108
———. 1992, Introduction to Stellar Astrophysics (Cambridge: Cambridge Univ. Press)
Bretherton, C., et al. 1999, Quart. J. Roy. Meteor. Soc., 125, 391
Carruthers, D. J., & Hunt, J. C. R. 1986, J. Fluid Mech., 165, 475
Cattaneo, F., Brummell, N. H., Toomre, J., Malagoli, A., & Hurlburt, N. E. 1991, ApJ, 370, 282
Chan, K. L., & Sofia, S. 1987, Science, 235, 465
———. 1989, ApJ, 336, 1022
———. 1996, ApJ, 466, 372
Charbonnel, C., & Talon, S. 1999, A&A, 351, 635
Clayton, D. D. 1983, Principles of Stellar Evolution and Nucleosynthesis (Chicago: Univ. Chicago Press)
Colella, P., & Glaz, H. M. 1985, J. Comput. Phys., 59, 264
Colella, P., & Woodward, P. 1984, J. Comput. Phys., 54, 174
Cox, J. P., & Giuli, R. T. 1968, Principles of Stellar Structure (New York: Gordon & Breach)
Dearborn, D. S. P., Lattanzio, J. C., & Eggleton, P. P. 2006, ApJ, 639, 405
Deardorff, J. W. 1979, J. Atmos. Sci., 36, 424
———. 1980, J. Atmos. Sci., 37, 131
Eggleton, P. P., Dearborn, D. S. P., & Lattanzio, J. 2007, in IAU Symp. 239, Convection in Astrophysics, ed. F. Kupka, I. W. Roxburgh, & K. Lam Chan (Cambridge: Cambridge Univ. Press), 286
Fedorovich, E. E., Conzemius, R., & Mironov, D. V. 2004, J. Atmos. Sci., 61, 281
Fedorovich, E. E., & Mironov, D. V. 1995, J. Atmos. Sci., 52, 83
Fernando, H. J. S. 1991, Annu. Rev. Fluid Mech., 23, 455
Fernando, H. J. S., & Hunt, J. C. R. 1997, J. Fluid Mech., 347, 197
Ferraro, F. R., Valenti, E., Straniero, O., & Origlia, L. 2006, ApJ, 642, 225
Freytag, B., Ludwig, H.-G., & Steffan, M. 1996, A&A, 313, 497
Fryxell, B., Müller, E., & Arnett, D. 1991, ApJ, 367, 619
García López, R. J., & Spruit, H. C. 1991, ApJ, 377, 268
Glatzmaier, G. A. 1984, J. Comput. Phys., 55, 461

Gough, D. O. 1969, J. Atmos. Sci., 26, 448
Grevesse, N., & Sauval, A. J. 1998, Space Sci. Rev., 85, 161
Hansen, C. J., & Kawaler, S. D. 1994, Stellar Interiors (Berlin: Springer)
Heger, A., Langer, N., & Woosley, S. E. 2000, ApJ, 528, 368
Heger, A., Woosley, S. E., & Spruit, H. C. 2005, ApJ, 626, 350
Herwig, F., Bloecker, T., Schoenberner, D., & El Eid, M. 1997, A&A, 324, L81
Herwig, F., Freytag, B., Hueckstaedt, R. M., & Timmes, F. X. 2006, ApJ, 642, 1057
Hoyle, F. 1946, MNRAS, 106, 343
Iglesias, C., & Rogers, F. J. 1996, ApJ, 464, 943
Itoh, N., Hayashi, H., Nishikawa, A., & Kohyama, Y. 1996, ApJS, 102, 411
Kantha, L. H., Phillips, O. M., & Azad, R. S. 1977, J. Fluid Mech., 79, 753
Kim, Y.-C., Fox, P. A., Demarque, P., & Sofia, S. 1996, ApJ, 461, 499
Kim, Y.-C., Fox, P. A., Sofia, S., & Demarque, P. 1995, ApJ, 442, 422
Kippenhahn, R., & Weigert, A. 1990, Stellar Structure and Evolution (Berlin: Springer)
Kuhlen, M., Woosley, S. E., & Glatzmaier, G. A. 2006, ApJ, 640, 407
Kupka, F., & Robinson, F. J. 2007, MNRAS, 374, 305
Langer, N., Fricke, K. J., & Sugimoto, D. 1983, A&A, 126, 207
Lattanzio, J. C., & Lugaro, M. A. 2005, Nucl. Phys. A, 758, 477
Lesaffre, P., Podsiadlowski, P., & Tout, C. A. 2005, MNRAS, 356, 131
Lilly, D. K. 2002a, J. Atmos. Sci., 59, 3340
———. 2002b, J. Atmos. Sci., 59, 3353
Linden, P. F. 1975, J. Fluid Mech., 71, 385
McGrath, J. L., Fernando, H. J. S., & Hunt, J. C. R. 1997, J. Fluid Mech., 347, 235
Meakin, C., & Arnett, D. 2006, ApJ, 637, L53
———. 2007, ApJ, 655, 690
Montalban, J. 1994, A&A, 281, 421
Pasquini, L., Bonifacio, P., Randich, S., Galli, D., & Gratton, R. G. 2004, A&A, 426, 651
Phillips, O. M. 1966, The Dynamics of the Upper Ocean (Cambridge: Cambridge Univ. Press)
Pinsonneault, M. H., Kawaler, S. D., Sofia, S., & Demarque, P. 1989, ApJ, 338, 424
Porter, D. H., & Woodward, P. R. 2000, ApJS, 127, 159
Porter, D. H., Woodward, P. R., & Jacobs, M. L. 2000, Ann. NY Acad. Sci., 898, 1
Press, W. H. 1981, ApJ, 245, 286
Rauscher, T., & Thielemann, K.-F. 2000, At. Data Nucl. Data Tables, 75, 1
Rempel, M. 2004, ApJ, 607, 1046
Ribas, I. 2006, in ASP Conf. Ser. 349, Astrophysics of Variable Stars, ed. C. Sterken & C. Aerts (San Francisco: ASP), 55
Robinson, F. J., Demarque, P., Guenther, D. B., Kim, Y.-C., & Chan, K. L. 2005, MNRAS, 362, 1031
Robinson, F. J., Demarque, P., Li, L. H., Sofia, S., Kim, Y.-C., Chan, K. L., & Guenther, D. B. 2003, MNRAS, 340, 923
———. 2004, MNRAS, 347, 1208

Rogers, T. M., & Glatzmaier, G. A. 2005a, ApJ, 620, 432
———. 2005b, MNRAS, 364, 1135
Shu, F. H. 1992, The Physics of Astrophysics, Vol. II: Gas Dynamics (Sausalito: University Science Books)
Smagorinsky, J. S. 1963, Monthly Weather Rev., 91, 99
Sorbjan, Z. 1996, J. Atmos. Sci., 53, 101
Spruit, H. C. 1992, A&A, 253, 131
———. 2002, A&A, 381, 923
Stevens, B. 2002, Quart. J. Roy. Meteor. Soc., 128, 2663
Stevens, D. E., & Bretherton, C. S. 1999, Quart. J. Roy. Meteor. Soc., 125, 425
Strang, E. J., & Fernando, H. J. S. 2001, J. Fluid Mech., 428, 349
Stull, R. B. 1973, J. Atmos. Sci., 30, 1092
———. 1976a, J. Atmos. Sci., 33, 1260

Stull, R. B. 1976b, J. Atmos. Sci., 33, 1268
Styne, I., Porter, D. H., Woodward, P. R., Hodson, S. H., & Winkler, K. H. 2000, J. Chem. Phys., 158, 225
Tennekes, H. 1973, J. Atmos. Sci., 30, 558
Timmes, F. X., & Swesty, F. D. 2000, ApJS, 126, 501
Turner, J. S. 1980, Buoyancy Effects in Fluids (Cambridge: Cambridge Univ. Press)
Unno, W., Osaki, Y., Ando, H., Saio, H., & Shibahashi, H. 1989, Nonradial Oscillations of Stars (2nd ed.; Tokyo: Univ. Tokyo Press)
Young, P. A., & Arnett, D. 2005, ApJ, 618, 908
Young, P. A., Knierman, K. A., Rigby, J. R., & Arnett, D. 2003, ApJ, 595, 1114
Zahn, J.-P. 1991, A&A, 252, 179